Pair distribution analysis of short- and medium-range order of metallic glasses: Direct imaging and diffraction-based approaches

Sangjun Kang,* Hyeyoung Cho, Takeshi Egami, Yuxuan Liao, Jianwei Miao, and Christian Kübel*

Pair distribution function (PDF) analysis provides a quantitative framework for resolving short- and medium-range order in glasses. This article summarizes recent advances that extend PDF methods from bulk x-ray and neutron-diffraction methods to local electron microscopy-based characterization for metallic glasses. High-energy x-rays and neutrons offer robust structural averages, while electron-based approaches such as electron PDF (ePDF) enable nanoscale mapping of local order and heterogeneity in metallic glasses. Validated PDF techniques, supported by molecular dynamics simulations, allow direct correlation between real-space pair correlations and the underlying atomic configurations. In particular, ePDF mapping visualizes nanoscale variations in short-range order (SRO), interfacial amorphous phases, and deformation-induced structural changes. Machine learning-assisted analysis enhances the extraction of meaningful structural motifs from large ePDF data sets. Complementary three-dimensional (3D) imaging methods, including atomic electron tomography and ptychography, allow to reconstruct coordinate-resolved 3D atomic models, which can be directly compared with atomistic simulations and can be evaluated locally via PDF analysis. This article provides an overview over recent methodology advances and further introduces possibilities to link multiscale PDF-derived structural information with properties and functionality in metallic glasses.

Motivation

Metallic glasses are structurally disordered alloys that lack long range periodicity, but display pronounced short- and medium-range order (S/MRO).[1] Their atomic structure is commonly described in terms of local coordination motifs, packing of polyhedra, and the way these motifs interconnect over nanometer length scales.[2–4] Their properties, including strength, plastic flow, and relaxation dynamics are highly sensitive to these local correlations. A quantitative description of S/MRO is therefore essential for understanding and designing metallic glasses.

Pair distribution function (PDF) analysis has been a central tool for characterizing S/MRO.[5–8] By describing the probability of finding atomic pairs as a function of distance, PDF provides direct access to nearest-neighbor coordination, bond length distributions, structural motifs, and medium-range density correlations up to several nanometers.[1,4,5,9] Advances in high-energy x-ray sources and synchrotrons now enable diffraction measurements that yield high-quality bulk PDFs for reliable pair correlations and robust coordination metrics with well-controlled systematic errors, providing reliable S/MRO information. When integrated with modeling approaches such as reverse Monte Carlo

Sangjun Kang, Institute of Nanotechnology (INT), Karlsruhe Institute of Technology (KIT), 76344 Eggenstein-Leopoldshafen, Germany; In-Situ Electron Microscopy, Department of Materials Science, Technical University of Darmstadt (TUDa), 64287 Darmstadt, Germany; Karlsruhe Nano Micro Facility (KNMFi), Karlsruhe Institute of Technology (KIT), 76344 Eggenstein-Leopoldshafen, Germany; sangjun.kang@tu-darmstadt.de
Hyeyoung Cho, Institute of Nanotechnology (INT), Karlsruhe Institute of Technology (KIT), 76344 Eggenstein-Leopoldshafen, Germany; In-Situ Electron Microscopy, Department of Materials Science, Technical University of Darmstadt (TUDa), 64287 Darmstadt, Germany; hyeyoung.cho@tu-darmstadt.de
Takeshi Egami, Department of Materials Science and Engineering, The University of Tennessee, Knoxville, Knoxville, USA; Department of Physics and Astronomy, The University of Tennessee, Knoxville, Knoxville, USA; Materials Science and Technology Division, Oak Ridge National Laboratory, Oak Ridge, USA; egami@utk.edu
Yuxuan Liao, Department of Physics and Astronomy and California NanoSystems Institute, University of California, Los Angeles, Los Angeles, USA; whuarxuan@gmail.com
Jianwei Miao, Department of Physics and Astronomy and California NanoSystems Institute, University of California, Los Angeles, Los Angeles, USA; j.miao@ucla.edu
Christian Kübel, Institute of Nanotechnology (INT), Karlsruhe Institute of Technology (KIT), 76344 Eggenstein-Leopoldshafen, Germany; In-Situ Electron Microscopy, Department of Materials Science, Technical University of Darmstadt (TUDa), 64287 Darmstadt, Germany; Karlsruhe Nano Micro Facility (KNMFi), Karlsruhe Institute of Technology (KIT), 76344 Eggenstein-Leopoldshafen, Germany; christian.kuebel@kit.edu
*Corresponding author
doi:10.1557/s43577-026-01120-z

(RMC),[10–13] empirical potential structure refinement (EPSR),[14–16] or molecular dynamics (MD),[17–21] PDF analysis provides stringent constraints on feasible atomistic configurations and facilitates quantitative testing of structure–property relationships across various metallic glass systems. However, obtaining a comprehensive structural picture from average pair correlations in the bulk alone remains challenging. Different local configurations can lead to very similar average scattering signatures, chemically complex alloys produce overlapping partial correlations, and nanoscale heterogeneities in density or topology are easily washed out in volume averaged measurements.

These difficulties have driven the development of experimental approaches that expand PDF analysis beyond conventional bulk total scattering. Electron-based methods, in particular nanobeam electron diffraction can confine the probe to nanometer sized volumes, enabling local ePDF analysis.[22–28] In combination with scanning transmission electron microscopy (STEM), four-dimensional (4D) STEM enables spatially resolved ePDF mapping and direction-sensitive pair-distribution analysis, which together capture changes in coherence length and structural anisotropy around defects, interfaces, and shear bands formed during deformation.[22,24–26]

In parallel, three-dimensional (3D) imaging methods such as atomic electron tomography and ptychographic phase retrieval have made it possible to reconstruct the 3D atomic structure of amorphous materials.[29,30] From these real space coordinates, one can compute PDF and related correlation measures that are directly comparable to atomistic simulations. Such coordinate resolved analyses provide a complementary view of S/MRO, highlighting connectivity of coordination polyhedra and spatial fluctuations in local packing.

This article focuses on PDF-based analysis of S/MRO in metallic glasses, with an emphasis on diffraction and direct imaging-based approaches. We discuss how bulk x-ray total scattering, local ePDF measurements based on 4D STEM, and atomic electron tomography can be used to extract PDFs, what assumptions and limitations are involved in each method, and how these techniques can be combined with simulations to obtain a consistent structural picture. We will further illustrate how the information obtained from the different pair distribution analysis approaches can help to understand materials aspects in metallic glasses research, such as thermodynamics of glass forming, glass-transition kinetics, and *in situ* processing pathways. This also includes possibilities for multimodal analysis enabling a direct correlation of PDF and functional analysis (e.g., characterizing local magnetic and/or strain fields). Our aim is to provide a practical framework for using PDF, measured across different length scales and modalities, to quantify S/MRO in metallic glasses.

Bulk total-scattering PDF as a probe of glass structure

In the absence of periodicity, the bulk structure of glasses and liquids is experimentally accessed primarily through their PDF that describes the distribution of atomic distances.[5] PDF analysis is as old as conventional crystallographic analysis of x-ray diffraction.[31] In 1913, Peter Debye suggested that the PDF can be directly determined by x-ray diffraction.[32] However, the experimental measurement of PDFs is more challenging than crystallographic diffraction measurements, because the structure signal is scattered over the entire reciprocal space, rather than just at Bragg peaks. This requires accurate subtraction of the background intensity, correction for absorption and multiple scattering, etc., to obtain the correctly normalized structure function, S(Q), where Q is the momentum transfer for scattering. The method is often called the total scattering method, because not only sharp Bragg peaks, but also diffuse background are used to construct the PDF.[32] For a long time, the method suffered inaccuracies due to the limited Q range that laboratory x-ray generators offer, which results in spurious termination errors, and was thus often discredited. However, this difficulty was largely eliminated by the advances in synchrotron radiation facilities, which provide intense high-energy x-rays. In a typical high-energy x-ray experiment carried out at a synchrotron facility, a monochromatic beam of the order of 100 keV with wavevector $\boldsymbol{k_i}$ is scattered by the sample into $\boldsymbol{k_s}$ at an angle 2θ, defining the scattering vector $\boldsymbol{Q} = \boldsymbol{k_s} - \boldsymbol{k_i}$; a 2D flat-panel detector records Debye–Scherrer rings that are azimuthally integrated to give I(Q) (**Figure 1**a). After standard corrections for background, absorption and instrument response, I(Q) is converted to the total structure function S(Q) and Fourier transformed to obtain the PDF, G(r) or g(r), defined by[5]

$$G(r) = 4\pi r\rho_0[g(r) - 1] = \frac{2}{\pi}\int_0^\infty [S(Q) - 1]\sin(Qr)QdQ. \quad (1)$$

As shown in Figure 1b–c, neutrons and x-rays give slightly different results, because of the different scattering amplitudes of neutrons and x-rays for each element. The atomic scattering factor for x-rays, $f(Q)$, decays with Q, but that for neutrons does not, providing more accurate information on $S(Q)$ at high Q values. With a reactor neutron source the range of Q is limited to about 12 Å^{-1}, but with a pulsed neutron source we can reach 50 Å^{-1} or beyond. This contrast provides some clue on chemical order. The scattering intensity of x-rays or neutrons is given by

$$S(Q) = \sum\nolimits_{\alpha,\beta} c_\alpha c_\beta f_\alpha(Q) f_\beta(Q) S^{\alpha\beta}(Q), \quad (2)$$

where α, β refer to chemical elements, c_α is the concentration of element α, $f_\alpha(Q)$ is the atomic scattering factor of element α, and $S^{\alpha\beta}(Q)$ is the partial structure function between α and β. The full analysis into compositionally resolved partial PDFs is impractical for metallic glasses with complex composition. But by using resonant scattering[34] for x-rays and isotropic substitution[35] for neutrons it is possible to determine the differential structure function, $S^\alpha(Q)$, defined by

$$S(Q) = \sum\nolimits_\alpha c_\alpha S^\alpha(Q), \quad S^\alpha(Q) = \sum\nolimits_\beta c_\beta S^{\alpha\beta}(Q). \quad (3)$$

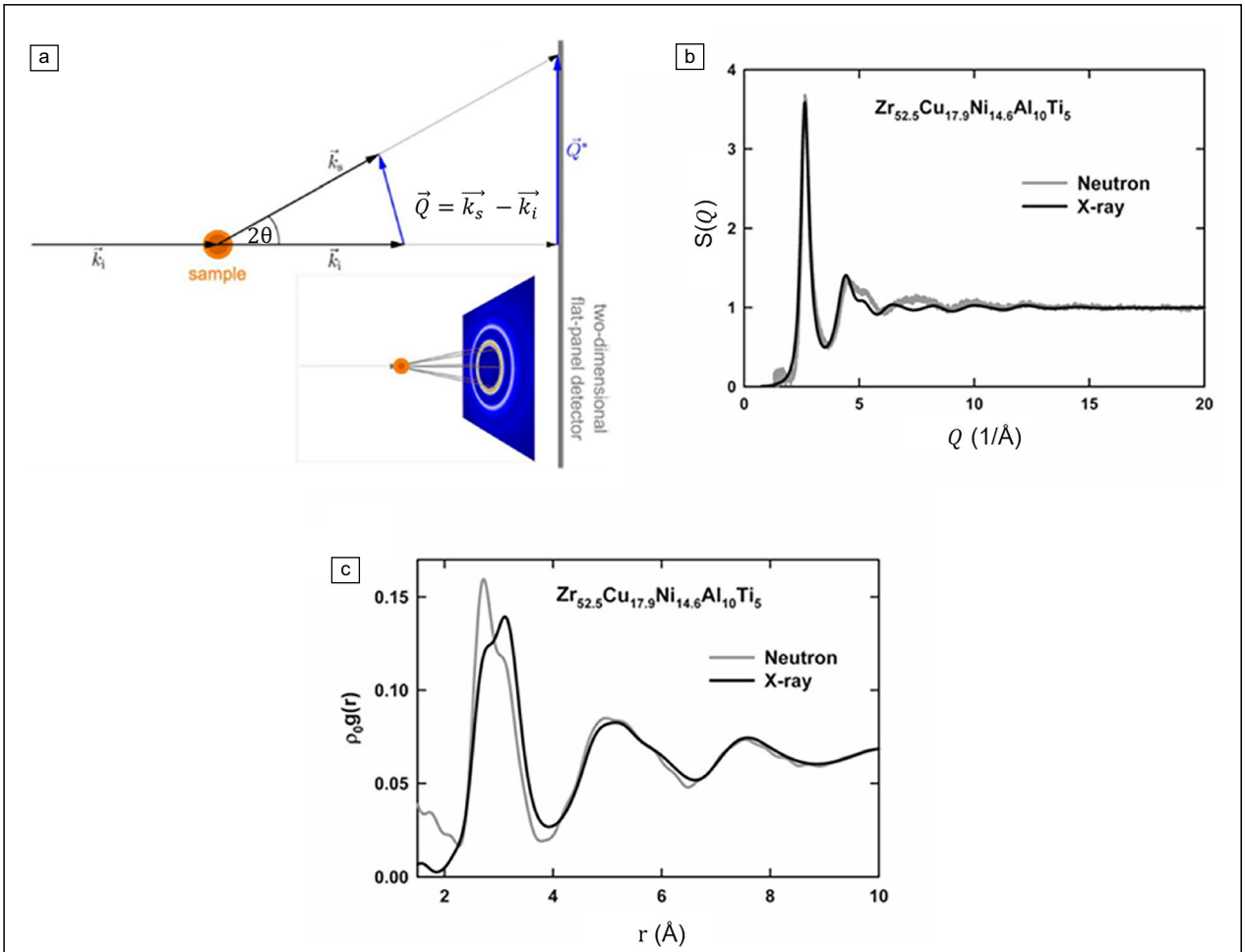

Figure 1. (a) High-energy x-ray total-scattering setup in transmission geometry: the incident beam with wave vector $\boldsymbol{k_s}$ is elastically scattered by the sample into $\boldsymbol{k_i}$ at angle 2θ, defining the scattering vector $\boldsymbol{Q} = \boldsymbol{k_s} - \boldsymbol{k_i}$. A two-dimensional flat-panel detector records concentric Debye–Scherrer rings (inset), which are azimuthally integrated to obtain I(Q) for pair distribution function (PDF) analysis. (b) The structural function S(Q) and (c) the PDF, for $Zr_{52.5}Cu_{17.9}Ni_{14.6}Al_{10}Ti_5$ glass, by neutron scattering (gray) and x-ray scattering (black).[33]

The Fourier transformation of $S^{\alpha}(Q)$ gives the differential PDF, the PDF centered on element α.

The resulting PDF can be interpreted in terms of bond lengths, coordination numbers, chemical short-range order, and medium-range correlations. It can be modeled either by real-space refinement against structural models or by reverse Monte Carlo and molecular dynamics approaches. Modeling can be made much more reliable when the differential PDFs are available, or both x-ray and neutron PDFs are determined. Otherwise, it is dangerous to determine the chemical identity by the peak position alone, because many peaks overlap in the PDF. From the first peak of G(r) or g(r) one can readily extract information on the average distance to the nearest-neighbor shell and the number of nearest-neighbor atoms, called the coordination number. This approach can be extended to the second neighbor shell as illustrated in **Figure 2**. However, beyond the second peak the number of pairs of atoms covered by each PDF peak becomes quite numerous. Thus, it is difficult to explain higher order PDF peaks in terms of the local structure. Yet, the PDF oscillations persist up to surprisingly long distances, covering several nanometers, indicating the presence of extended MRO.

Interestingly, these extended MRO oscillations are quite regular, representing just one frequency. Furthermore, the amplitude decays exponentially with distance, as

$$G(r) = G_0(r)\exp\left(-\frac{\xi_s(T)}{r}\right), \tag{4}$$

where $\xi_s(T)$ is the MRO coherence length, as shown in **Figure 3**.[36,37] Here, a $Pd_{42.5}Ni_{7.5}Cu_{30}P_{20}$ glass with complex chemistry, involving covalent bonds for P, exhibits very regular MRO oscillations similar to those of liquid Ar, suggesting that the MRO oscillations are insensitive to chemistry and local structure or bonding. Indeed, a study of the MRO oscillations in chemically resolved partial PDFs proves that the extended MRO oscillations are not sensitive to chemical composition.[38] Therefore, it is impossible to explain these oscillations in terms of combinations of local motifs. As was pointed

out by Cargill,[6] the MRO oscillations are almost totally determined by the first peak of S(Q), which is much taller and sharper than the other peaks of S(Q) as shown in Figure 1b. Its height is proportional to $\xi_s(T)$, whereas its width is inversely related to $\xi_s(T)$. Such sharp peaks are almost universally seen for all kinds of glasses and liquids, including inorganic and molecular glasses and liquids. They are called the "first sharp diffraction peak (FSDP).[39]"

If the FSDP cannot be explained through the "bottom-up" approach of starting from an atom and building up the local motifs, how can we elucidate such extended MRO correlations? A possible answer is the "top-down" approach, based on the density wave theory.[37,38,40,41] If we start with a high-density gas of non-interacting particles and introduce local interparticle interactions in real space, this leads to the formation of local clusters or motifs. However, if we instead introduce simultaneously an interaction with all particles, a long-range structure is obtained, which can be described by the density wave theory.[42] Utilizing a pseudopotential concept,[37] it was found that density waves with a wavevector Q_{DW}, which is close to the position of the first peak of S(Q), are formed as results of the interparticle interaction introduced in reciprocal space. In this density wave state, the MRO coherence length $\xi_s(T)$ is infinite. So, it has a long-range order and is no longer glassy. It is a quasicrystal with $3N$ order parameters, where N is the number of atoms in the system. Unlike the icosahedral quasicrystal,[43] it has no orientational order, and its model appears random and isotropic.[36] The PDF of this state is given by $G_0(r)$ in Equation 4. Details of this approach are discussed in References 44 and 45 and this issue.

In situ synchrotron experiments on metallic-glass-forming liquids demonstrate how the PDF evolves along the entire liquid-glass pathway within a single measurement. For example, high-energy x-ray diffraction on $Zr_{60}Cu_{20}Al_{10}$ shows that the first diffuse maximum in S(Q) gradually grows and shifts to slightly higher Q as the melt is cooled from the equilibrated liquid through T_g (**Figure 4**a). The corresponding reduced PDF g(r) exhibits a sharpening of the first-shell peak and an increase in the amplitude and coherence of the medium-range oscillations (Figure 4b), reflecting both a tightening of the spread of nearest-neighbor distances and the growth of MRO. An earlier measurement on a $Pd_{42.5}Ni_{7.5}Cu_{30}P_{20}$ alloy shows the height of the first-peak or integrated intensity in S(Q) (Figure 4c) as well as the MRO coherence length $\xi_s(T)$ (Figure 4d) to follow the Curie–Weiss Law,

$$\frac{\xi_s(T)}{a} = C\frac{T_g}{T - T_{IG}} \quad (T > T_g), \tag{5}$$

where a is the average nearest-neighbor distance and T_{IG} is the ideal glass temperature at which $\xi_s(T)$ diverges in extrapolation.[36] Below T_g $\xi_s(T)$ freezes to a constant value. Molecular dynamics simulations on various metallic alloy liquids show that the Curie–Weiss Law is universally obeyed for metallic liquids, as shown in Figure 4d.[46]

The MRO coherence length $\xi_s(T)$ can be directly related to viscosity,[36] liquid fragility,[48] and mechanical ductility.[21] In particular, it was shown that the activation energy for viscosity just above T_g is proportional to $\xi_s^3(T)$, the coherence volume. This suggests that the MRO coherence length $\xi_s(T)$ defines the range of dynamic cooperativity in supercooled liquids. For this reason, it is an important parameter that controls various properties of supercooled liquids.[44] The Curie–Weiss Law shows that $\xi_s(T)$ becomes longer as a liquid is cooled, suggesting that there is a driving force toward the state with infinite $\xi_s(T)$, the density wave state. In reality, a liquid never reaches this state, because $\xi_s(T)$ freezes at T_g and also T_{IG} is negative. Nevertheless, the presence of such a driving force toward the density wave state is a compelling argument for the need for a top-down approach.[37] The Curie–Weiss Law, Equation 5, was quantitatively explained in terms of local structural volume fluctuations.[45]

A related line of work uses bulk PDF to probe how deformation modifies the glassy state.[47] When stress is applied to a metallic glass, its structure becomes anisotropic. In the absence of the periodic lattice, it is not easy to characterize the effect of stress on the local structure. The best way is to expand S($\boldsymbol{Q}$) and g($\boldsymbol{r}$) by spherical harmonics $Y_\ell^m(\boldsymbol{z})$ as,

$$S(\boldsymbol{Q}) = \sum\nolimits_{\ell,m} S_\ell^m(Q) Y_\ell^m\left(\frac{\boldsymbol{Q}}{Q}\right), \quad g(\boldsymbol{r}) = \sum\nolimits_{\ell,m} g_\ell^m(r) Y_\ell^m\left(\frac{\boldsymbol{r}}{r}\right). \tag{6}$$

They are connected through the spherical Bessel transformation,

$$g_\ell^m(r) = \frac{1}{2\pi^2 r}\int S_\ell^m(Q) J_\ell(Qr) Q^2 dQ, \tag{7}$$

where J_ℓ is the spherical Bessel function. For the affine (homogeneous) uniaxial deformation along the z-axis, it can be shown that $g_2^0(r)$ is given by

$$g_{2,affine}^0(r) = -\epsilon\left(\frac{1}{5}\right)^{\frac{1}{2}} \frac{2(1+\nu)}{3} r\frac{d}{dr} g_0^0(r). \tag{8}$$

However, even for apparently elastic deformation, $g_2^0(r)$ measured experimentally deviates significantly from Equation 6. So, it is useful to define the r-dependent strain

$$g_2^0(r) = -\epsilon(r)\left(\frac{1}{5}\right)^{\frac{1}{2}} \frac{2(1+\nu)}{3} r\frac{d}{dr} g_0^0(r). \tag{9}$$

As shown in Figure 4e–f, $\varepsilon(r)$ is less than the average strain $\varepsilon(\infty)$ at the nearest neighbors even for elastically deformed sample. The non-affine deformation zone extends further in a sample creep deformed by applying stress at an elevated temperature. This non-affine strain results from the local structural relaxation to accommodate the applied stress by local atomic rearrangements.

It is interesting to note that even elastic stress well below the elastic limit induces local plastic atomic rearrangements in

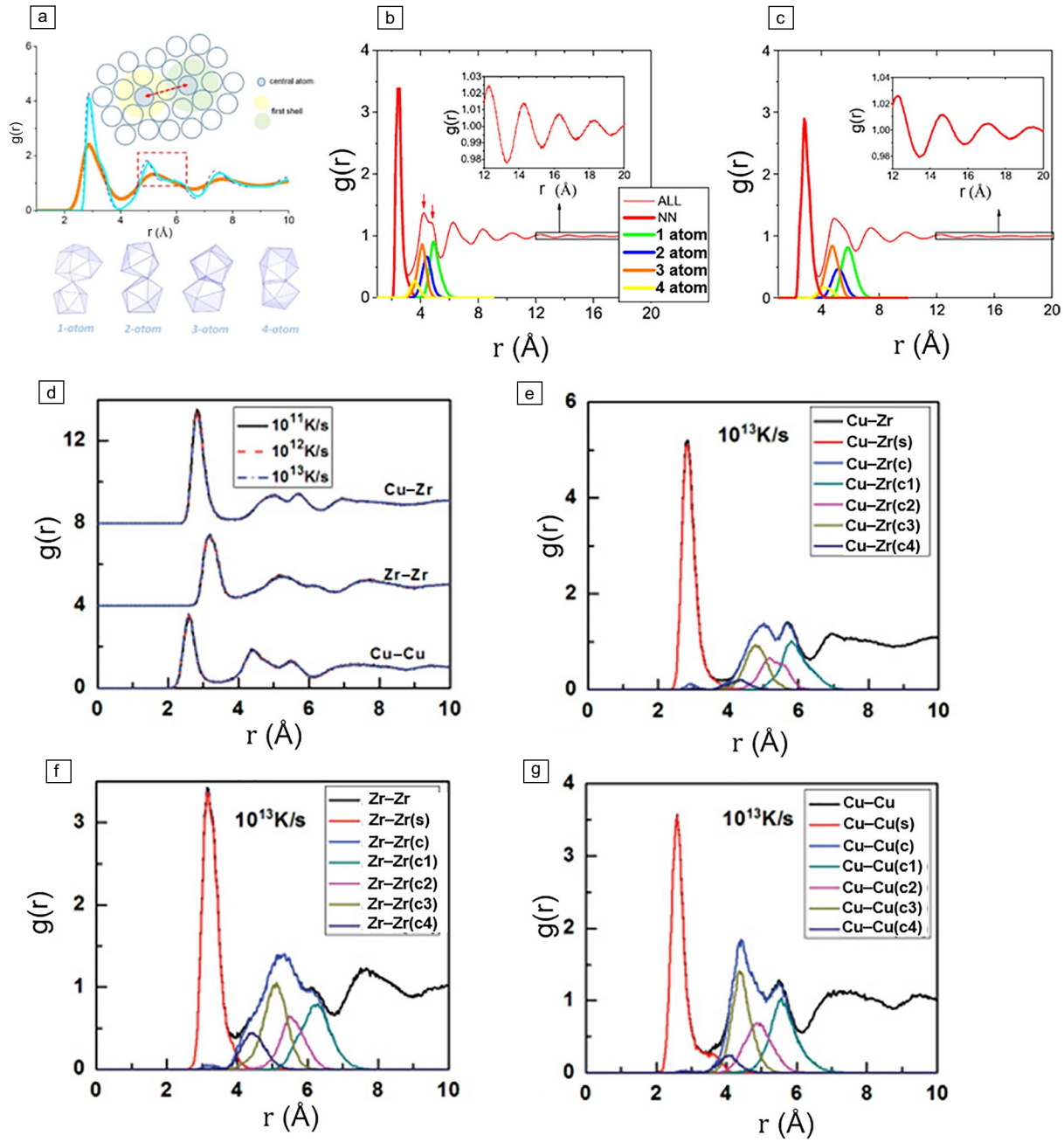

Figure 2. Cluster-connection analysis of the origin of the second-peak splitting in metallic-glass pair distribution functions (PDFs). (a) Schematic illustration of how atoms in the second-neighbor shell arise from connections between coordination polyhedra that share one, two, three, or four atoms with a central cluster. (b) Decomposition of the total PDF g(r) into contributions from the nearest-neighbor shell (NN) and from 1-, 2-, 3- and 4-atom-shared connections, showing that an unequal population of these connection types reproduces the characteristic splitting of the second maximum. (c) Example of the same analysis for a higher-density glassy state, highlighting the enhancement of face-sharing (three-atom-shared) connections on vitrification. (d) Partial PDFs $g_{Cu–Zr}(r)$, $g_{Zr–Zr}(r)$, and $g_{Cu–Cu}(r)$ for a $Cu_{50}Zr_{50}$ metallic glass obtained from molecular dynamics simulations at different cooling rates, demonstrating that the second-peak splitting is essentially insensitive to quench rate. (e–g) Decomposition of the Cu–Zr, Zr–Zr, and Cu–Cu partial PDFs for a rapidly quenched glass into contributions from the first shell $g_{\alpha\beta}(s)$ and from connections where the corresponding coordination polyhedra share $i = 1$–4 atoms, $g_{\alpha\beta}(c–i)$. Three-atom-shared connections dominate the low-r subpeak, while one-atom-shared connections contribute mainly to the high-r subpeak. Adapted with permission from Reference 17. © 2011 American Physical Society.

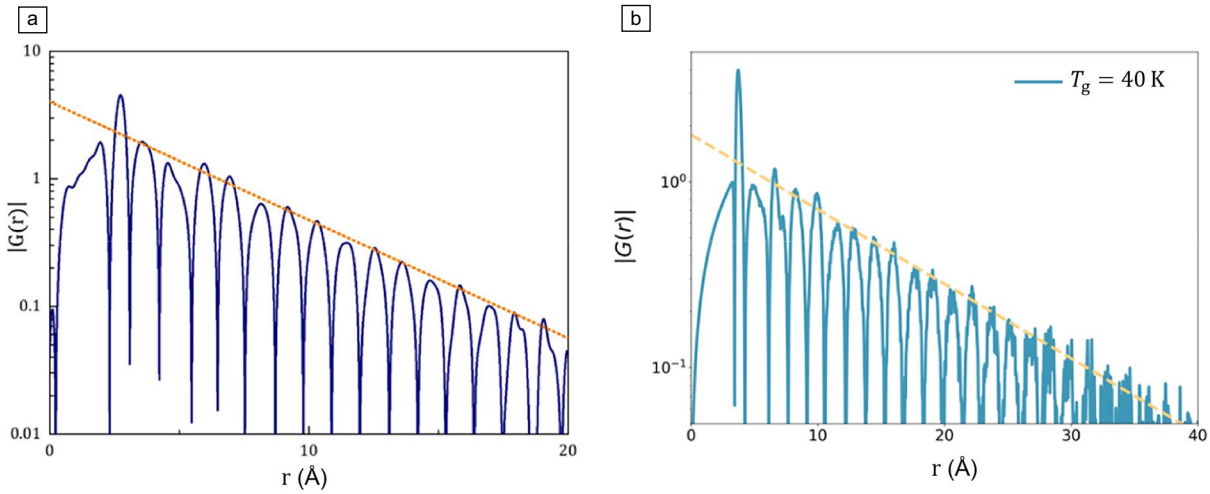

Figure 3. Exponential decay of the medium-range order oscillations for (a) $Pd_{42.5}Ni_{7.5}Cu_{30}P_{20}$ glass at 600K by x-ray diffraction[33] and (b) Ar liquid at 40 K by simulation.[36]

metallic glasses.[49] This is evidence that a glass is not totally frozen, and locally some liquid-like states remain.[44] Such residual liquidity results in mechanical loss down to $T = 0$ due to quantum mechanical tunneling,[50] connecting it to the two-level states (TLS) universally found in glasses.[51] The origin of these liquid-like states is closely tied to the mechanism of the glass transition. Because the number of the nearest neighbors is finite (12–13), a certain minimum strain is required to change the local coordination.[33] In terms of the volume strain, this critical strain is $\epsilon_v^{crit} = 11$.[52] This defines "liquid-like" atoms of which atomic-level volume strain exceeds ϵ_v^{crit}, thus intrinsically unstable. If the glass transition occurs by the loss of percolation of liquid-like atoms,[53] about 20% of atoms remain liquid-like even after a liquid freezes into a glass.[33] These left-over liquid-like atoms provide the residual liquidity in glasses.

Local characterization of metallic glasses via ePDF

Methodology of ePDF

In ePDF total scattering analysis is applied to nanometer-scale volumes recorded in a TEM.[27,28,54] The basic workflow follows similar steps as in x-ray and neutron-diffraction-based PDF analysis. Diffraction patterns are first corrected for the detector response and integrated azimuthally to obtain radial intensity profiles I(k). k denotes the electron scattering vector, defined as $k = 2 \sin \theta/\lambda$, where θ is half the scattering angle and λ is the electron wavelength. In the traditional x-ray and neutron PDF literature, the scattering vector is usually written as $q = 4\pi \sin \theta/\lambda$. The two conventions are therefore related by $k = q/2\pi$. Throughout this text, q is used when referring to conventional x-ray PDF, and k is used for electron diffraction. Each profile is normalized using the total elastic scattering factor to give the structure function S(k). The reduced structure function $F(k) = k\,[S(k) - 1]$ is then Fourier transformed over a selected k range to obtain G(r), which describes deviations of the local atomic density from the average as a function of distance as introduced above for x-ray-based PDF analysis.

The main complication compared to x-ray and neutron-based PDF is the strong interaction of electrons with matter.[55,56] Even for amorphous foils that are only a few tens of nanometers thick, electrons undergo significant multiple elastic scattering. In reciprocal space this appears as a thickness-dependent diffuse background, a mismatch between the fitted atomic scattering factor and the measured I(k) that leads to a low-frequency background of S(k). In real space, these effects generate artificial intensity especially at small r, but also shift the first coordination peak to smaller distances, and attenuate or broaden oscillations associated with the MRO.

The basic strategy for treating these effects is illustrated in **Figure 5**. Starting from the diffraction profile I(k), the single-atom scattering contribution $f(k)^2$ is removed and the intensity is normalized to obtain the total structure function S(k). Multiple scattering mostly appears as a smooth background on which the true structural oscillations are observed. To remove this, a low-order polynomial (red curve in Figure 5) is fitted to the background and subtracted, leaving only the oscillatory part of S(k). A careful choice of polynomial order is required to avoid either residual baseline curvature or over-subtraction of genuine structural signals, both of which can bias peak positions in G(r). Practical guidance on selecting the polynomial order and assessing thickness-related peak shifts is provided by Kang et al.[57]

Kang et al. showed that, even with a reasonably chosen polynomial background correction, the extracted G(r) still exhibits a gradual shift of the first peak toward lower r with increasing sample thickness.[57] This can be attributed to multiple scattering, which redistributes electrons toward higher

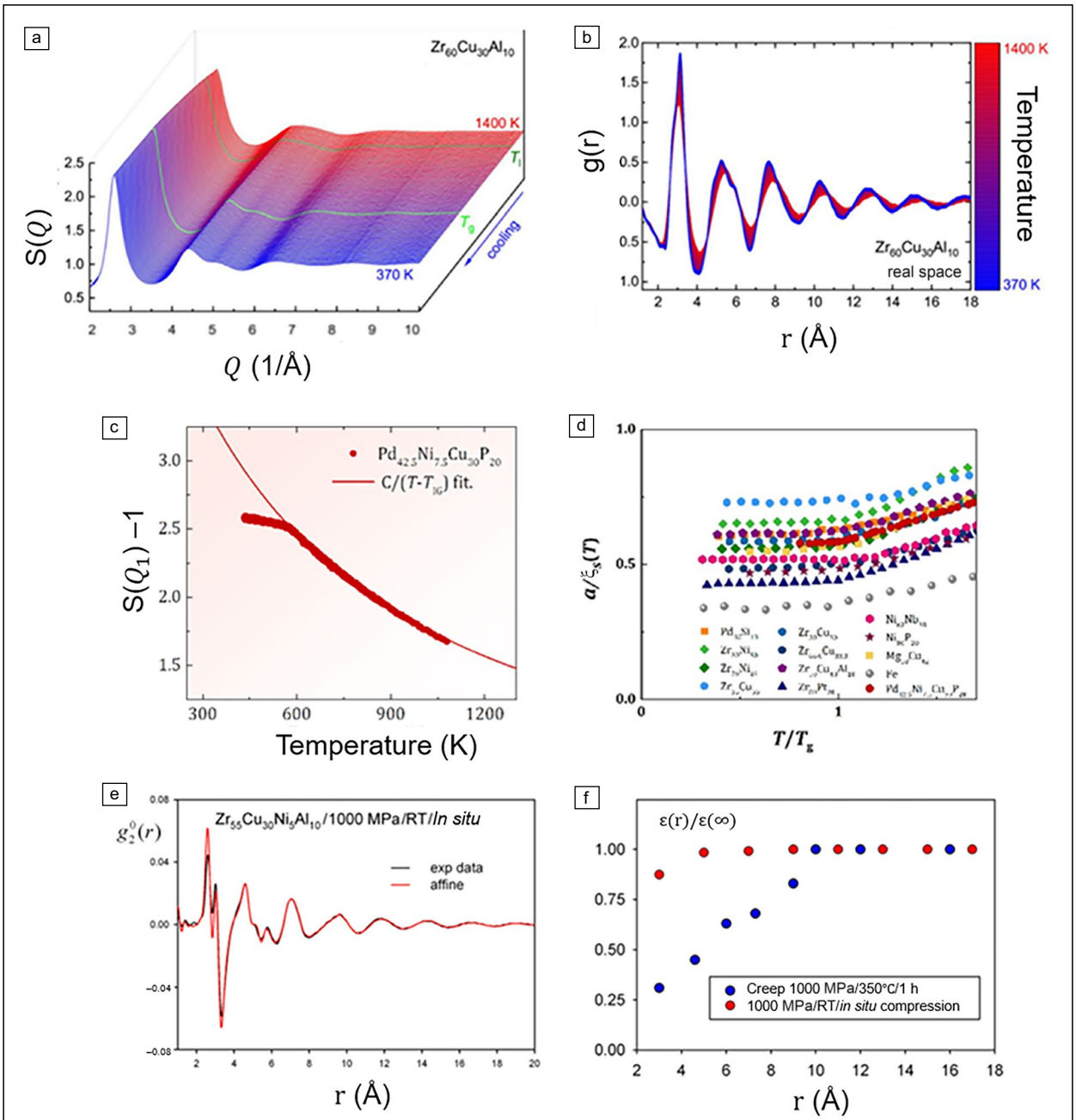

Figure 4. (a) Temperature-resolved structure factor S(Q) plotted as a surface versus Q and T, showing the growth and slight outward shift of the first diffuse maximum on cooling, obtained by *in situ* high-energy x-ray diffraction on a $Zr_{60}Cu_{30}Al_{10}$ alloy during cooling from the equilibrium liquid through the glass transition. (b) Corresponding reduced pair distribution function g(r), whose first-shell peak sharpens and medium-range oscillations become more pronounced as the liquid approaches the glassy state.[36] (c) Temperature evolution of the height of the first diffuse maximum, $S(Q_1)-1$, for $Pd_{42.5}Ni_{7.5}Cu_{30}P_{20}$ liquid measured by electrostatic-levitation high-energy x-ray diffraction, following a Curie–Weiss Law in the equilibrium liquid.[36] (d) Temperature evolution of the inverse of the medium-range order coherence length, $\xi_s(T)$, for various metallic alloy liquids, where *a* is the average nearest-neighbor distance.[46] (e) $g_2^0(r)$ under the stress of 1 GPa compared to that for affine deformation by Equation 5, (f) *r*-dependent strain, ε(r), for elastic deformation (red circle) at RT (room temperature) and creep deformation (blue circle).[47]

scattering angles and produces shoulders on the diffraction peaks, so that the apparent first-peak position decreases by about 1% as the thickness increases from 20 to 100 nm, accompanied by a reduction in peak height and a nonlinear change in width.

To address the physical origins of multiple elastic scattering and its influence on ePDF, Kang et al. adopted the analytical deconvolution originally developed by Anstis and co-workers.[55,56] A deconvolution framework can be applied to efficiently compensate for the multiple scattering impact on ePDF, yielding

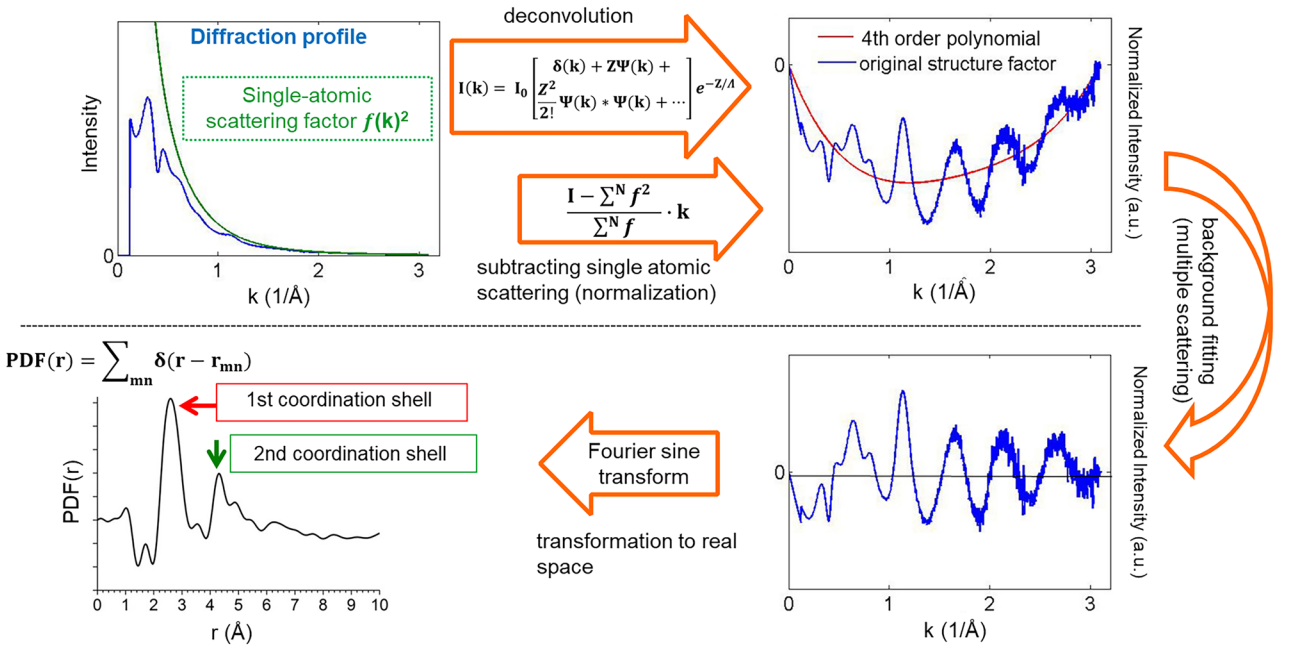

Figure 5. Schematic workflow for electron pair distribution function (ePDF) data processing. Multiple-scattering deconvolution is applied to the measured diffraction intensity, I(k), obtained from the raw 2D diffraction pattern after detector correction and azimuthal integration. The deconvolved intensity is then normalized by the single-atom scattering factor, *f*(k),[2] to obtain the total structure function, S(k). A low-order polynomial background is subsequently fitted and subtracted to remove the remaining low-frequency background, yielding the oscillatory part of S(k). The reduced structure function, $F(k) = k[S(k) - 1]$, is then Fourier sine transformed to obtain the real-space PDF, G(r), from which the first and second coordination shells can be identified. Adapted with permission from Reference 28 with permission. © 2013 International Union of Crystallography.

highly accurate peak positions, as quantitatively analyzed and illustrated for an amorphous Pd-Si glass in **Figure 6**c–f. In this formalism, the measured intensity I(k) is written as a Poisson-weighted sum of self-convolutions of an effective single-scattering distribution Ψ(k), with the weights depending on the specimen thickness *Z* and the elastic mean free path Λ. Assuming azimuthal symmetry for amorphous materials, a Fourier–Bessel transform converts I(k) into a radial representation in which the Poisson series can be inverted via a logarithmic relation, allowing the single-scattering distribution to be recovered. Transforming back to reciprocal space yields a corrected I(k) dominated by single scattering. Kang et al. showed that, after this deconvolution, the thickness-dependent shifts of the shoulders in S(k) are largely removed and the first peak of ePDF fully collapses onto the ground truth (Figure 6c and d). The remaining smooth background can then be removed with a low-order polynomial (first to third order), as quantified in Figure 6e. With this combined deconvolution plus baseline correction, the first peak in G(r) becomes essentially thickness-independent (within about 0.001 Å over the tested thickness range), and the variations in peak height and width with thickness are strongly reduced (Figure 6f). In addition to multiple scattering and background correction, the fidelity of ePDF is strongly influenced by the electron-optical and acquisition conditions. Small to moderate convergence semi-angles preserve angular resolution and MRO in G(r), whereas overly large angles blur the oscillations in S(k) and broaden the peaks. Sufficient detector sampling and an appropriately chosen k range and Fourier window are likewise essential to avoid aliasing and truncation artifacts, so that ePDF peak positions and medium-range oscillations remain consistent with bulk x-ray and neutron PDFs while retaining nanometer-scale spatial resolution.

The different scattering contrasts further define the strengths of each approach. Bulk x-ray PDFs provide statistically robust structural averages with high reciprocal-space resolution, especially at synchrotron sources, but the x-ray atomic form factor decreases with increasing scattering vector and the total PDF is weighted approximately by electron density. Neutron PDFs provide complementary element-specific contrast because neutron scattering lengths are element- and isotope-dependent and do not decrease with scattering vector in the same way as x-ray form factors. Electron PDFs offer strong scattering and nanometer-scale spatial resolution, making them particularly useful for interfaces, shear bands, nanoglasses and other locally heterogeneous structures, but they require careful control of multiple scattering and specimen thickness.

STEM-PDF for nanoscale structural mapping

The capability of 4D STEM-PDF for nanoscale structural mapping has been demonstrated both for amorphous organic films and metallic glasses (**Figure 7**).[27,58,59] In a typical workflow, a nanometer-sized probe is scanned across the specimen,

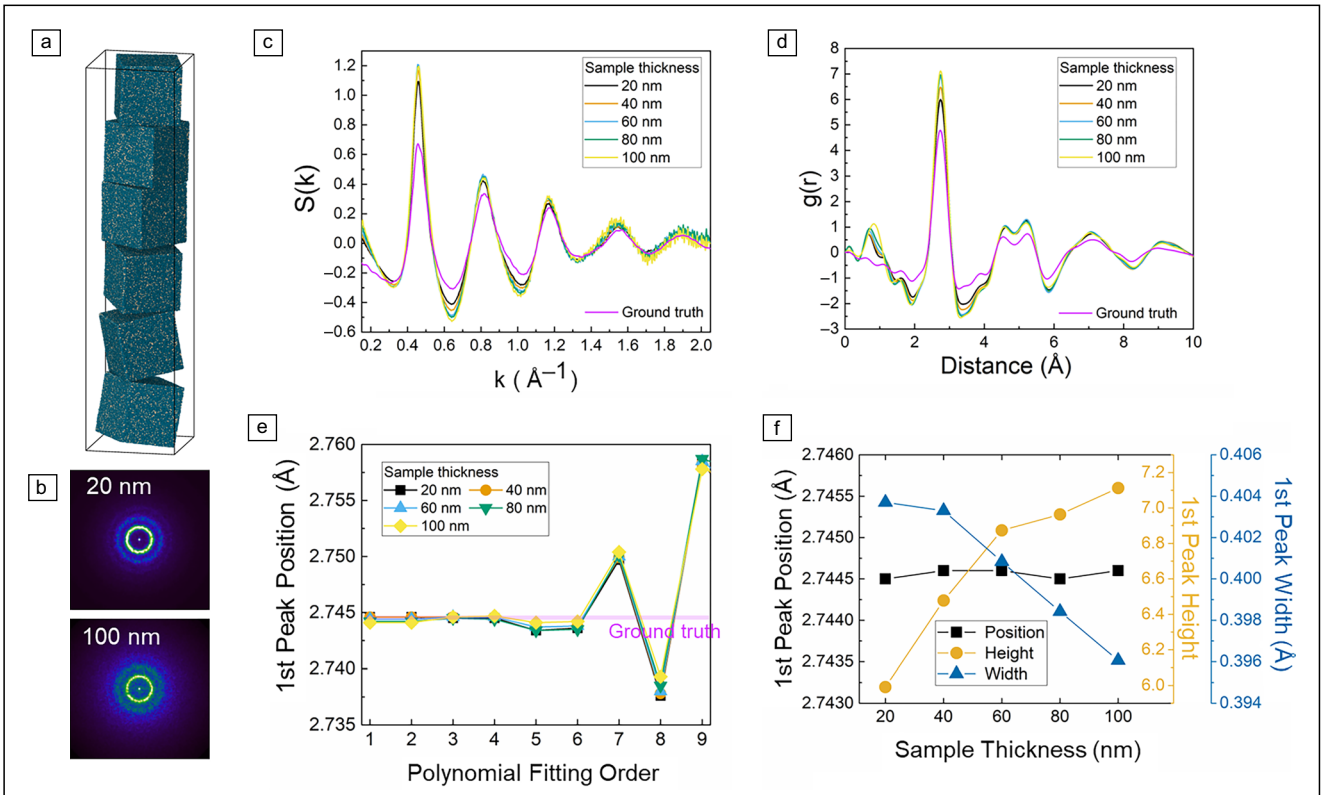

Figure 6. Influence of sample thickness and polynomial baseline correction on electron pair distribution function (ePDF) after deconvolution. (a) Stacked $Pd_{80}Si_{20}$ atomic models are used to simulate increasing thickness and (b) the corresponding selected-area electron diffraction (SAED) patterns for 20-nm and 100-nm samples. (c) Structure factors S(k) for thicknesses of 20–100 nm after deconvolution, showing thickness-dependent low-frequency background from residual multiple scattering, compared to the ground-truth kinematic S(k). (d) Resulting ePDFs for different thicknesses obtained from the deconvolved S(k). (e) First-peak position in g(r) as a function of polynomial fitting order, illustrating overfitting at high orders even after deconvolution. (f) First-peak position, height, and width as a function of sample thickness after deconvolution and polynomial baseline correction, demonstrating systematic thickness effects on ePDF metrics. Adapted with permission from Reference 57. © 2025 Elsevier.

while a 2D detector records a diffraction pattern at each position, generating a 4D data set. Each pattern is processed as described in the "Methodology of ePDF" section to calculate the corresponding ePDF. Stacking the local ePDFs over the scan grid yields a 3D "PDF cube" with two spatial coordinates (x, y) and one real-space axis r(Figure 7a). Mu et al. first used this approach to map structural heterogeneity in metallic glass multilayers and amorphous organic semiconductors, revealing nanometer-scale phase separation and morphology that are difficult to access by conventional imaging while simultaneously providing quantitative local pair-correlation information.[27,59]

As a proof of principle for metallic and oxide glass multilayers, 4D STEM-PDF of ZrFe/ZrO_2 multilayers resolved distinct S/MRO signatures associated with different amorphous regions.[59] The PDFs contain features attributable to Zr–O, Fe–Fe, Fe–Zr, and Zr–Zr distances, enabling phase identification (Figure 7b). By fitting representative PDFs to the PDF cube, Mu et al. constructed coefficient maps that delineate the ZrFe and ZrO_2, thereby visualizing nanoscale phase distributions and interfacial amorphous layers (Figure 7c).[59] Mu et al. subsequently extended 4D STEM-PDF from mapping to a multivariate framework capable of separating overlapping amorphous phases in projection (Figure 7d–h).[58] In this approach, the PDF cube is reshaped into a matrix where rows correspond to probe positions and columns to discrete r values. Principal component analysis (PCA) is used for denoising and to estimate the number of significant components using a modified scree criterion that combines eigenvalues with a local-entropy measure of the component maps.[58] Because PCA components can remain mixtures of distinct amorphous environments, independent component analysis (ICA) is then applied to rotate the PCA subspace into statistically independent components that are interpreted as PDFs of individual nanophases.[58] Applied to the amorphous ZrO_2/FeZr multilayer, this PCA-ICA workflow yielded three independent PDFs and coefficient maps: two matched the FeZr and ZrO_2 layers, while the third showed Fe–O and Fe–Fe correlations consistent with a marokite-type Fe_3O_4 model.[58] The corresponding coefficient map revealed a thin, highly overlapped Fe_3O_4-like interlayer, demonstrating that multivariate decomposition of STEM-PDF data can uncover hidden nanophases and recover their local bonding geometry. The differences in atomic packing and MRO between core and interfacial regions yielded a spatial resolution on the order of 2–3 nm (**Figure 8**).

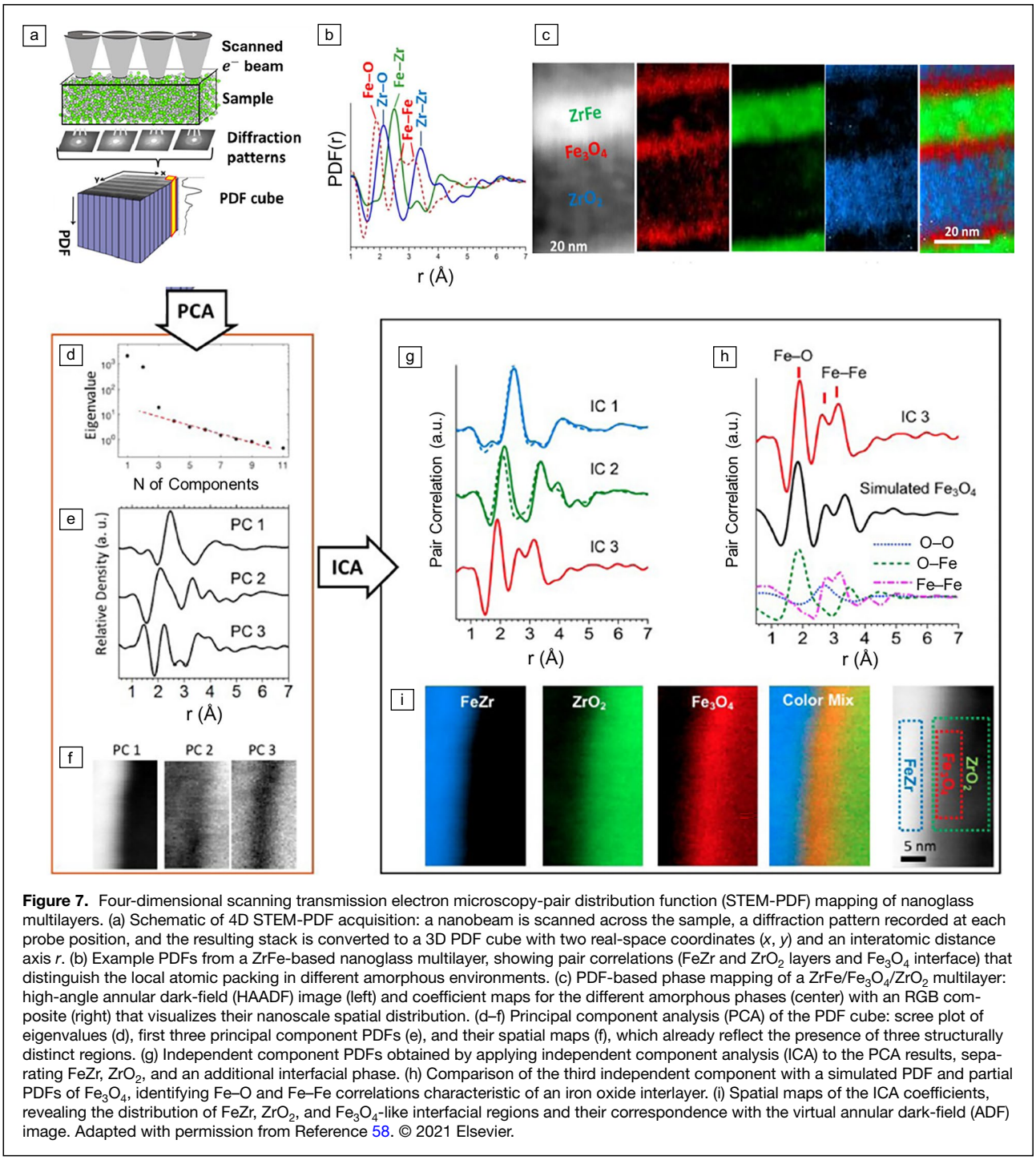

Figure 7. Four-dimensional scanning transmission electron microscopy-pair distribution function (STEM-PDF) mapping of nanoglass multilayers. (a) Schematic of 4D STEM-PDF acquisition: a nanobeam is scanned across the sample, a diffraction pattern recorded at each probe position, and the resulting stack is converted to a 3D PDF cube with two real-space coordinates (x, y) and an interatomic distance axis r. (b) Example PDFs from a ZrFe-based nanoglass multilayer, showing pair correlations (FeZr and ZrO_2 layers and Fe_3O_4 interface) that distinguish the local atomic packing in different amorphous environments. (c) PDF-based phase mapping of a ZrFe/Fe_3O_4/ZrO_2 multilayer: high-angle annular dark-field (HAADF) image (left) and coefficient maps for the different amorphous phases (center) with an RGB composite (right) that visualizes their nanoscale spatial distribution. (d–f) Principal component analysis (PCA) of the PDF cube: scree plot of eigenvalues (d), first three principal component PDFs (e), and their spatial maps (f), which already reflect the presence of three structurally distinct regions. (g) Independent component PDFs obtained by applying independent component analysis (ICA) to the PCA results, separating FeZr, ZrO_2, and an additional interfacial phase. (h) Comparison of the third independent component with a simulated PDF and partial PDFs of Fe_3O_4, identifying Fe–O and Fe–Fe correlations characteristic of an iron oxide interlayer. (i) Spatial maps of the ICA coefficients, revealing the distribution of FeZr, ZrO_2, and Fe_3O_4-like interfacial regions and their correspondence with the virtual annular dark-field (ADF) image. Adapted with permission from Reference 58. © 2021 Elsevier.

In 4D STEM structure mapping, "machine learning" is commonly used in a broad sense to denote data-driven statistical methods for dimensionality reduction and signal separation in large diffraction data cubes. Unsupervised decomposition or clustering (e.g., NMF, PCA/ICA-type approaches) are applied to diffraction-derived representations such as azimuthally averaged diffraction profiles or ePDFs to extract a small number of recurring components and their spatial weight maps, which serve as quantitative maps of selected structural descriptors related to local order, clustering, or compositional SRO. These tools primarily provide a systematic and reproducible way to compress and segment high-dimensional data. Physical interpretation still requires connecting the extracted components to established structural metrics, simulations, or complementary experiments. As one example, Rakita et al. introduced the scanning nanostructure electron microscopy

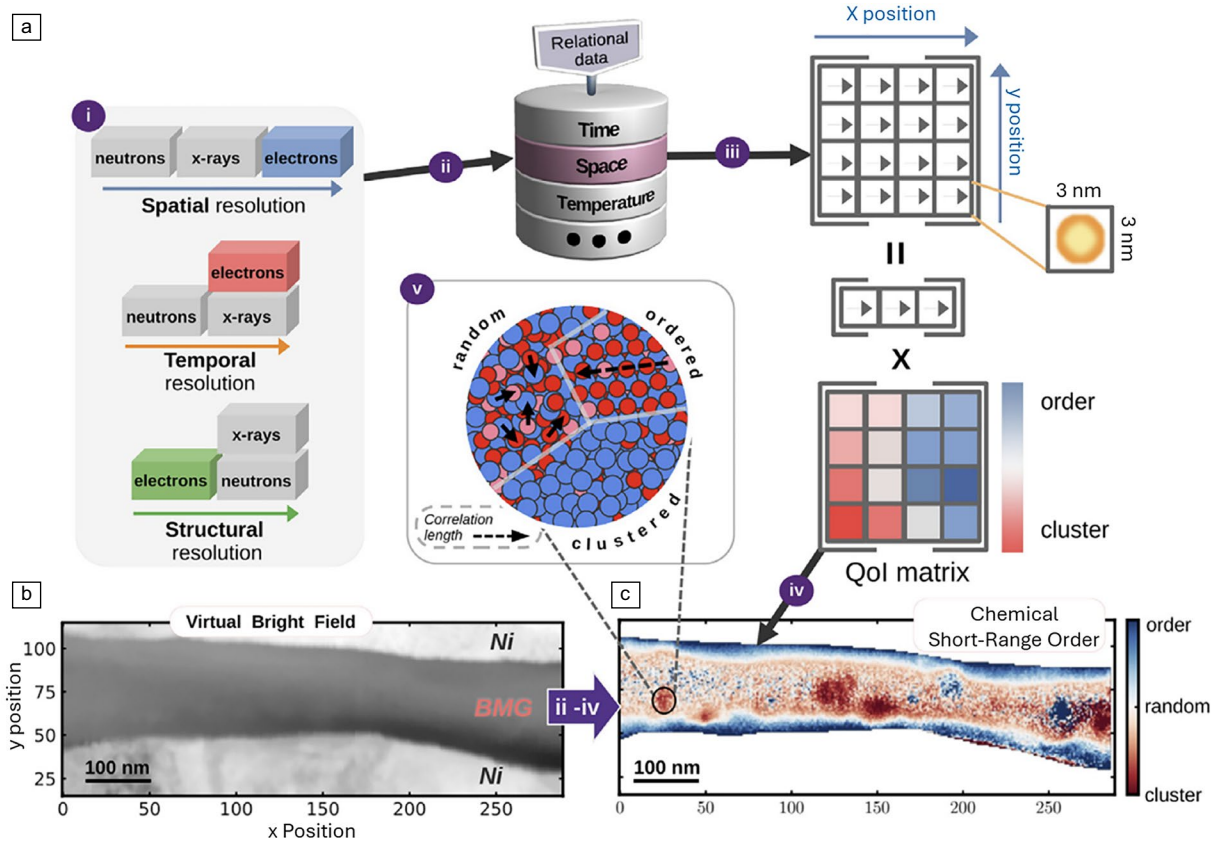

Figure 8. Data-driven analysis workflow for mapping nanoscale order from 4D scanning transmission electron microscopy (STEM) diffraction data. (a) Schematic workflow converting a 4D STEM data set (a diffraction pattern recorded at each probe position) into spatial maps of selected quantities of interest (QoIs). Electron probes provide high spatial sampling; the diffraction patterns can be reduced to 1D profiles (e.g., electron pair distribution functions [ePDFs]) and analyzed using statistical decomposition methods (e.g., nonnegative matrix factorization) to obtain component signals and their spatial weights. The resulting QoIs are assembled on the scan grid to visualize heterogeneity in local order or clustering (illustrated here for chemical short-range order). (b) Virtual bright-field image of a Ni/BMG(bulk metallic glass)/Ni laminate indicating the region used for analysis. (c) Example QoI map across the BMG layer showing spatial variations from random-like to clustered or more ordered motifs at nanometer-scale sampling. Adapted with permission from Reference 60. © 2021 Elsevier.

(SNEM) framework, in which a 4D STEM data set is converted into a set of local 1D ePDFs and analyzed with simple unsupervised, data-driven tools to produce spatial maps of structural "quantities of interest" (QoIs).[60] They used correlation-based similarity mapping and nonnegative matrix factorization (NMF) to segment the ePDF cube into a small number of recurring component PDFs and their coefficient maps. Several NMF components could be interpreted as partial pair-correlation contributions, allowing the corresponding coefficient maps to be viewed as approximate "bond maps" and further condensed into a chemical short-range order (CSRO) map that highlights nanoscale heterogeneity, especially near interfaces and nucleation sites.

Kang et al. employed NMF-based 4D STEM-PDF analysis to identify structural bases of metallic glasses directly from the PDF cubes (**Figure 9**a).[24] NMF decomposes this cube into a small set of basis PDFs H_i and corresponding weight maps from the ePDF cube. Because NMF enforces nonnegativity, each measured PDF is represented as an additive mixture of the basis PDFs, which makes the extracted bases easy to interpret as physically meaningful local structural types rather than abstract mathematical modes. The decomposition yields two dominant basis PDFs with clearly different S/MRO, shown as H_1 and H_2 in Figure 9a. The first basis has a slightly larger first neighbor distance and broader peaks, while the second basis shows shorter interatomic distances and sharper first and second peaks. By relating the second-peak positions and shoulders to different polyhedron connection schemes, Kang et al. found that H_2 corresponds to more efficiently packed motifs with a larger number of shared atoms, whereas H_1 contains less efficiently packed motifs with more free volume. Following liquid theory terminology, these two structural types were labeled as "liquid-like" and "solid like."

The physical meaning of these bases becomes clear when comparing as spun and flash annealed samples. As shown in Figure 9b, d, the liquid-like and solid-like basis PDFs obtained

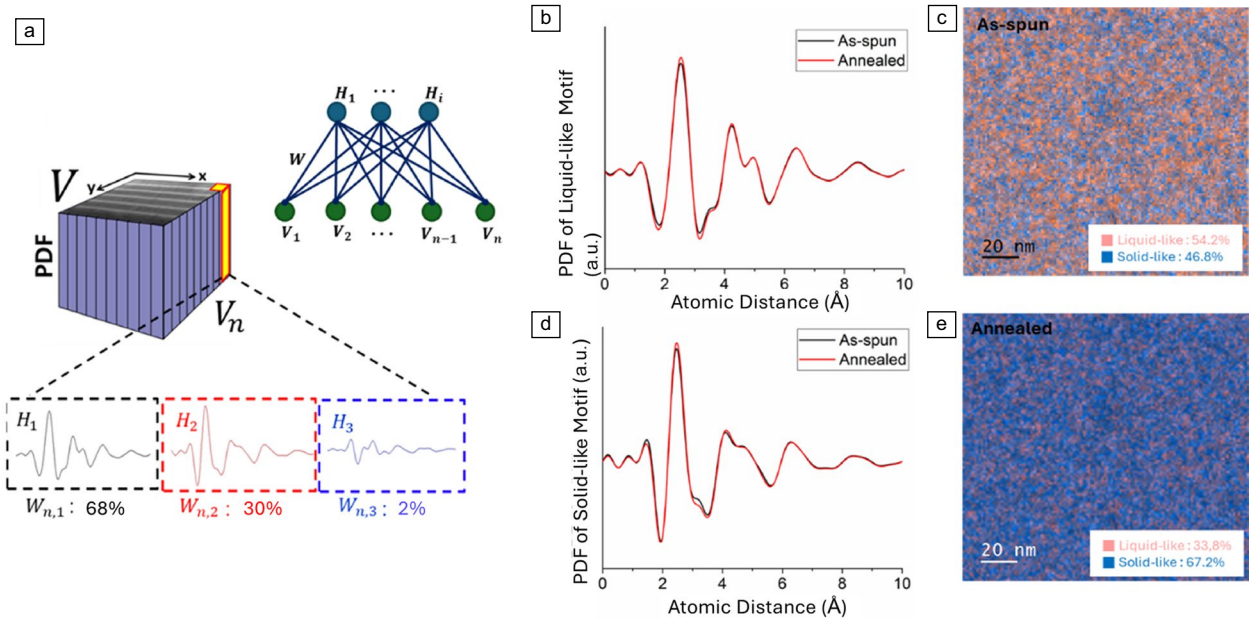

Figure 9. Nonnegative matrix factorization (NMF) aided 4D scanning transmission electron microscopy-pair distribution function (STEM-PDF) analysis of an Fe-based metallic glass. (a) A 4D STEM scan is converted into a local PDF cube, which is decomposed by a neural network style NMF model into a small number of basis PDFs H_1, H_2 and H_3 and their weights. (b) Basis PDFs associated with the liquid-like structural types independently extracted from as-spun and annealed $Fe_{85.2}Si_{0.5}B_{9.5}P_4Cu_{0.8}$ metallic glass; the nearly identical curves show that the underlying local atomic configurations are preserved upon annealing. (c) Maps of the liquid-like (orange) and solid-like (blue) structural types for the as-spun glass, together with their areal fractions. (d) Basis PDFs associated with the solid-like structural types independently extracted from as-spun and annealed $Fe_{85.2}Si_{0.5}B_{9.5}P_4Cu_{0.8}$ metallic glass; the nearly identical curves show that the underlying local atomic configurations are preserved upon annealing. (e) Maps of the liquid-like (orange) and solid-like (blue) structural types for the annealed glass together with their areal fractions. Adapted with permission from Reference 24. © 2024 Elsevier.

from the two states nearly overlap, demonstrating that annealing near the glass transition does not create new structural motifs but preserves the underlying local configurations. However, annealing redistributes their populations. NMF coefficient maps in Figure 9c, e show that liquid-like and solid-like regions are intermixed throughout the glass with a characteristic correlation length of about 5–6 nm, consistent with earlier nanobeam studies of structural heterogeneity. Quantitative analysis of these maps reveals that the fraction of solid-like structure increases from roughly 47% in the as-spun ribbon to about 67% after annealing, while the fraction of liquid-like structure decreases correspondingly, in agreement with the idea that the energetically favorable structure is preferred during flash annealing.

While 4D STEM-PDF provides a direct, real-space resolved view of local structure through pair correlations, it is important to emphasize that the fact that any structural variations emerge in PDF coefficient maps of ≈100-nm-thick samples implies that similar local motifs are not randomly distributed, but instead organize into larger assemblies over nanometer length scales. In other words, real-space heterogeneity in PDF-derived metrics is a manifestation of higher-order structural organization that goes beyond purely two-body statistics. This directly connects 4D STEM-PDF with fluctuation electron microscopy (FEM), because FEM is explicitly designed to probe medium-range structural organization through higher-order correlations that are largely invisible in the average diffuse diffraction signal. FEM yields quantitative MRO descriptors as discussed in more detail by Voyles and Rösner et al. in References 61–66 and this issue.

Application to shear-band characterization

Mu et al. used STEM-based PDF mapping combined with ICA to resolve the local atomic structure changes across a shear band in a Vitreloy 105 metallic glass (**Figure 10**). A 4D STEM data set was acquired over a region containing a single shear band (SB) and converted into a local PDF map (Figure 10a). ICA of this map yielded two independent PDFs (IC1 and IC2) that can be assigned to Zr-rich and Zr-poor local configurations, based on their nearest-neighbor distances and comparison with MD-derived bond lengths (Figure 10b). The corresponding IC maps show that these two structural motifs form an antisymmetric pair of shear-band-affected zones (SBAZs) on either side of the SB: a Zr-depleted/Cu-rich zone on one side and a Zr-enriched zone on the other, separated by a narrow band where the fitting error is largest (Figure 10c–e). This demonstrates that shear banding modifies the local glass structure not only within the band, but also tens of nanometers into the surrounding matrix with a different response on the compressive and tensile side of the SB.

To probe the associated changes in S/MRO order, a line scan of PDFs perpendicular to the SB (Figure 10f–g) reveals a gradual shift of the Zr–Zr nearest-neighbor peak across the SBAZs,

(See figure on next page.)

Figure 10. Scanning transmission electron microscopy-pair distribution function (STEM-PDF) and independent component analysis (ICA) mapping of local atomic structure around a shear band (SB) of a Vitreloy 105 metallic glass. (a) STEM-high-angle annular dark-field (HAADF) image of a deformed section, indicating the region used for 4D STEM-PDF acquisition and the position of the SB. (b) Independent-component PDFs IC1 and IC2 obtained by independent component analysis (ICA) of the STEM-PDF cube, corresponding to Zr-rich (IC1) and Zr-poor (IC2, Cu/Ni/Ti/Al-rich) local configurations. (c, d) Spatial weight maps of IC1 and IC2, revealing a sharp structural contrast across the SB (yellow dashed line). (e) Line profile of the IC weight fractions and fitting error along the direction marked in (a), showing antisymmetric Zr-rich/Zr-poor shear-band-affected zones (SBAZs) on either side of the SB and a narrow region of enhanced misfit at the SB core. (f) PDF line scan perpendicular to the SB extracted from the STEM-PDF cube. (g) Magnified view of the line scan highlighting changes in the Zr–Zr nearest-neighbor distance and the second-shell feature associated with face-sharing tetrahedra; right-hand traces show intensity profiles in the Zr-depleted SBAZ, SB, and Zr-enriched SBAZ. (h) PDFs averaged over these three regions, illustrating the progressive change in nearest-neighbor correlations and the abrupt reduction of the face-sharing contribution in the SB. (i) Map of the population of face-sharing tetrahedral motifs derived from the PDF amplitude at $\sqrt{8/3}\,R_{NN}$, showing depletion of geometrically favored motifs along the SB. Adapted with permission from Reference 67. © 2021 Wiley.

reflecting compositionally driven changes in local packing over tens of nanometers and an abrupt drop of the shoulder of the second peak at about 4.8 Å exactly at the SB position. These compositionally driven S/MRO changes in the SBAZ are more localized than the MRO variations observed by FEM in Vitreloy 105 extending micrometers from the SB.[68] Directly at the SB, by relating the ratio of the first- and second-peak position in the PDF to different polyhedra-connection distances, a decrease in geometrically favored face-sharing tetrahedra could be identified in the SB, which indicates fragmentation of these densely packed motifs inside the SB during mechanical deformation.

Gammer et al. developed a 4D STEM-based strain-mapping approach for amorphous materials by quantifying the elliptic distortion of diffuse diffraction rings: at each probe position, the diffraction pattern is fitted by an ellipse, and elastic loading induces an elliptic distortion of the rings from which the local strain is extracted.[69] Applied to an *in situ* tensile test of a CuZr-based metallic glass, the method enabled visualization of a strongly heterogeneous elastic strain distribution with a spatial resolution of a few nanometers. During continuous loading, the tensile-direction elastic strain increased, and after catastrophic fracture a residual elastic strain field was observed that relaxed over time, highlighting the ability of 4D STEM nanodiffraction to capture transient strain evolution in amorphous solids.

Building on this methodology, Kang et al. combined 4D STEM-based strain mapping with local ePDF analysis to directly correlate nanoscale stress fields with atomic structure in a deformed $Fe_{85.2}Si_{0.5}B_{9.5}P_4Cu_{0.8}$ metallic glass.[26] From the elliptic distortion of the diffuse diffraction rings, maps of deviatoric and volumetric strain can be reconstructed, while azimuthally averaged patterns from the same 4D STEM data can be converted into local PDFs to extract the nearest-neighbor distance at each probe position for a multimodal analysis. This provides a fully correlative view of the residual strain field and local atomic packing around SBs in a thick TEM lamella (≈200 nm), where conventional high-resolution imaging and FEM would struggle because of multiple scattering and the projected sample volume. However, this high TEM sample thickness helps to maintain the bulk structure, whereas strain relaxation has been observed for significantly thinner FIB prepared samples.[70]

Figure 11b–e illustrates the key findings for a representative shear band (SB1). A vector field of the maximum shear strain overlaid on the volumetric strain map (Figure 11b) reveals a chain of vortex-like features along the SB. A magnified view shows that these vortices coincide with quadrupolar shear patterns and dilated regions in the nearest-neighbor distance map (Figure 11c): strain concentrates at the cores of Eshelby-like inclusions that sit at the center of quadrupolar strain fields and exhibit slightly larger atomic spacings than the surrounding matrix. Line profiles along the band (Figure 11d) quantify this correlation: the maxima of deviatoric strain, volumetric strain, and nearest-neighbor distance occur at the same positions, whereas the regions between inclusions show reduced strain and slightly shorter nearest-neighbor distances. The width of the sharp peaks in deviatoric strain is about 15 nm, providing an experimental upper bound for the projected size of the inclusion cores. PDFs averaged over inclusions, regions between inclusions, and the undeformed matrix (Figure 11e) show that the overall short- and medium-range order remains very similar, consistent with the amorphous nature of all regions. Nevertheless, statistically significant differences are small shifts of the first peak toward larger distance and a reduced peak height, indicating a reduced coordination number, at the inclusions compared with the compressed zones between inclusions and the matrix. Together with the volumetric strain map, this indicates that the inclusions correspond to locally dilated zones where the hydrostatic stress increases the average atomic spacing, while the areas between inclusions are slightly compressed. As the small Eshelby-like inclusions are clearly visible in projections of a 200-nm-thick sample, this raises the unanswered question of their 3D structure, if they are more extended in the projection direction.

Taken together, the shear-band studies by Mu et al. and Kang et al. should be viewed as complementary. Mu et al. combined STEM-PDF mapping and ICA with atom probe tomography (APT), which provided quantitative 3D composition information across the shear band and the shear-band-affected zones. The STEM-PDF/ICA resolved local structural components assigned to Zr-rich and Zr-poor configurations, while APT independently supported elemental partitioning

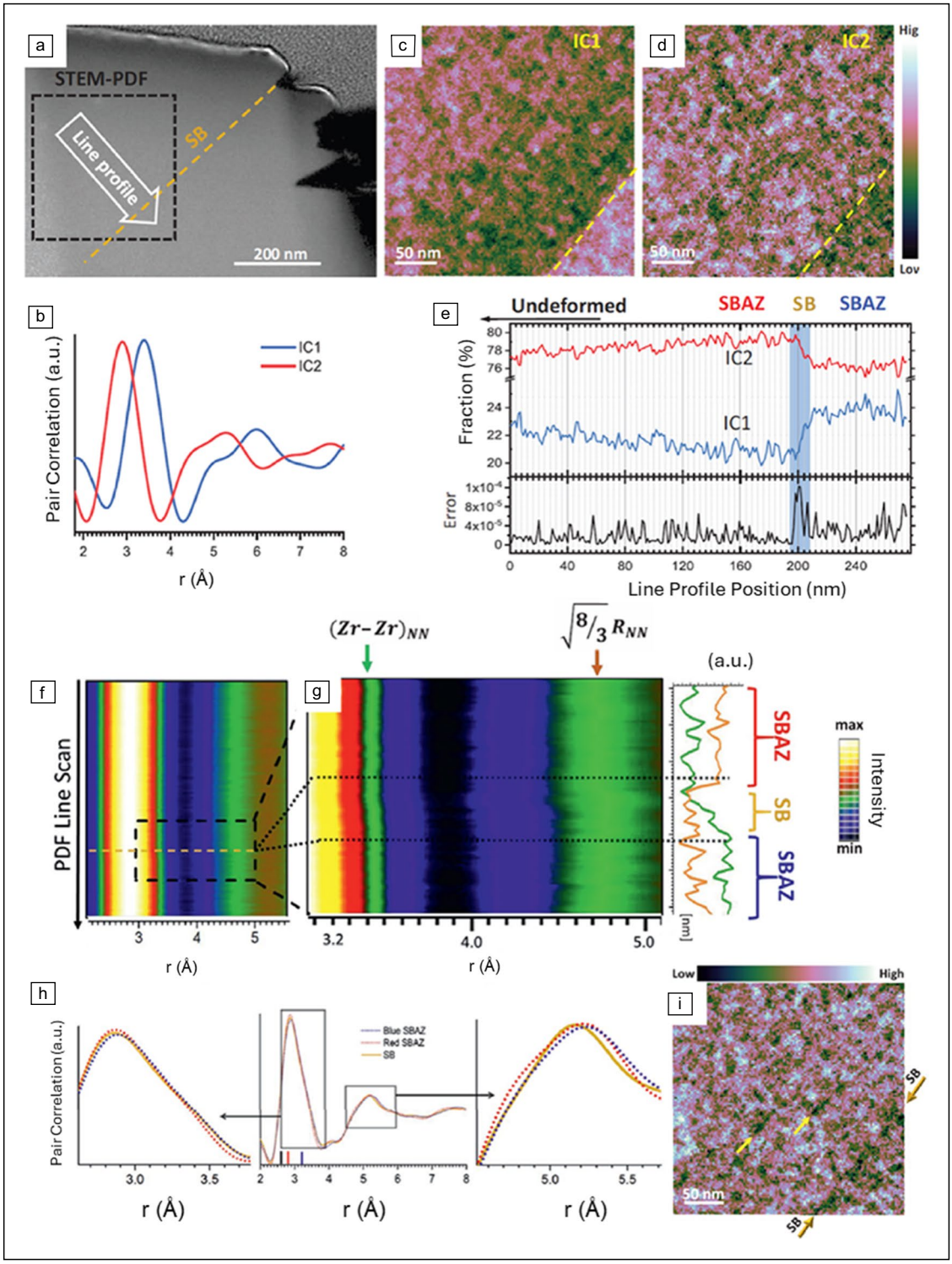

across the two sides of the shear band. This combination allowed Mu et al. to link changes in local pair correlations and SRO to measured elemental redistribution. In contrast, Kang et al. combined 4D STEM strain mapping with local ePDF analysis and focused primarily on mechanical and elastic heterogeneity around the shear band. Their measurements revealed Eshelby-like quadrupolar strain fields, local volumetric dilation, and small but statistically significant changes in nearest-neighbor distance and PDF peak height, without resolving a compositional gradient (within the sensitivity of their measurements). The difference between the two observations could therefore arise from differences in alloy chemistry,

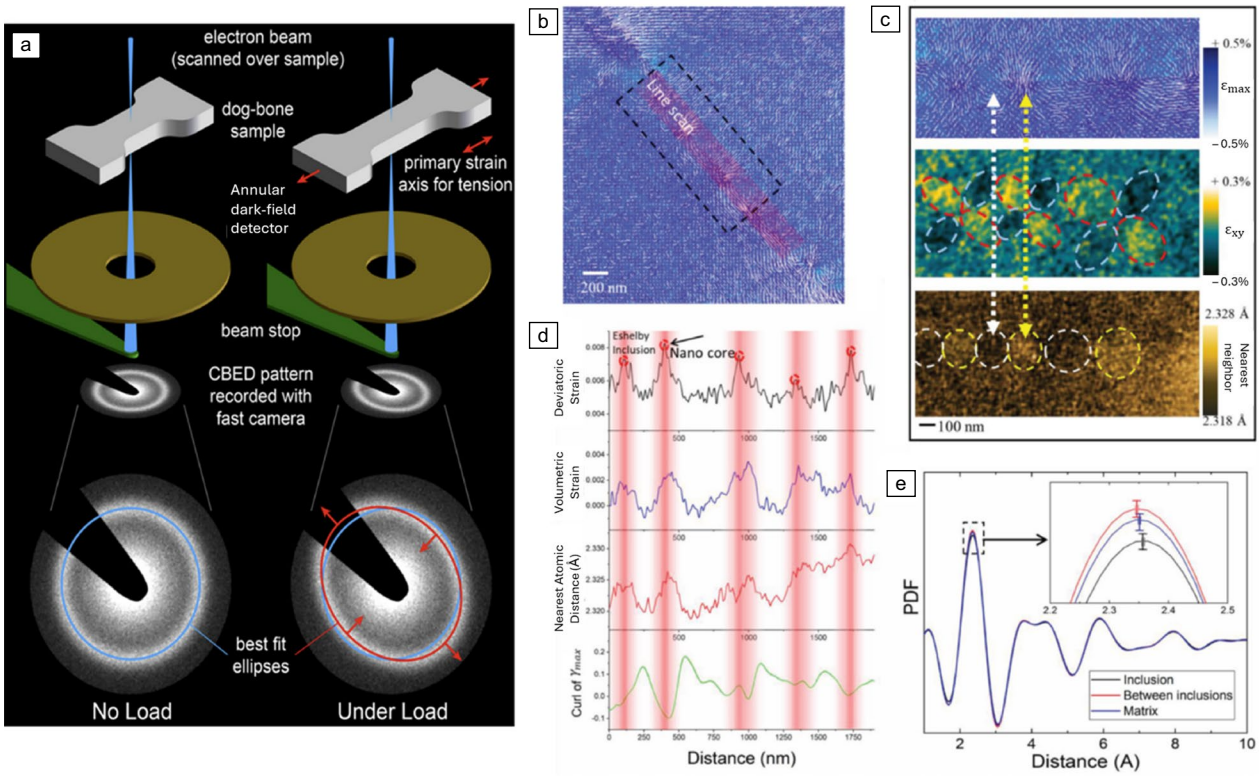

Figure 11. Correlative 4D scanning transmission electron microscopy (STEM) strain and pair distribution function (PDF) mapping of Eshelby-like inclusions along a shear band in a deformed $Fe_{85.2}Si_{0.5}B_{9.5}P_4Cu_{0.8}$ metallic glass. (a) Experimental geometry for 4D STEM strain mapping. At each probe position, a convergent-beam electron diffraction (CBED) pattern is recorded and fitted with a best-fit ellipse; elastic loading induces an elliptic distortion of the rings, from which local strain is quantified. (b) Vector-field map of the maximum shear strain γ_{max} overlaid on the volumetric strain ϵ_{vol}. The dashed box marks the region used for quantitative line analysis. (c) Magnified view of the boxed area showing ϵ_{vol} (top), shear strain ϵ_{xy} (middle), and nearest-neighbor distances (bottom) derived from 4D STEM. Dashed circles highlight dilated Eshelby-like inclusions located at the center of the quadrupolar strain fields. (d) Line profiles along the shear band of deviatoric strain, volumetric strain, nearest-neighbor distance, and curl of γ_{max}; red shaded bands denote the position of inclusions and their nanocores, where strain and nearest-neighbor distance reach local maxima. (e) PDFs averaged over typical inclusions, regions between inclusions and the undeformed matrix, with the inset showing the first peak, revealing small but statistically relevant increase in nearest-neighbor distance and reduction in peak height (coordination number) at the inclusions, consistent with local dilatation. (a) Adapted from Gammer et al.[69] (b–e) Adapted from Kang et al.[26]

deformation history, specimen thickness, projection geometry as well as differences in sensitivity of the characterization methods. Nevertheless, both studies suggest that shear bands in metallic glasses are not uniform planar defects, but structurally heterogeneous zones in which elemental redistribution, SRO, motif connectivity, free volume, and residual strain could evolve in different combinations.

Toward functional analysis

In addition to the pure structural analysis, Kang et al. recently showed that 4D STEM can be extended to simultaneously provide functional information. In the large-angle Lorentz 4D STEM analysis of a Fe-based metallic glass (**Figure 12**), the same 4D data set is used to reconstruct the in-plane magnetic field from shifts of the amorphous diffraction ring, the elastic strain tensor from its distortions, and the relative mass density from the integrated intensity. The resulting maps reveal how shear bands reorganize not only the atomic packing but also the local magnetization and strain state on the few nanometer scale (Figure 12a–e). Statistical analysis of the strain and magnetic-field orientations (Figure 12f–i) reveals regions where the field is primarily constrained by the shear-band geometry and regions dominated by magnetostatic interactions. To connect these functional maps to the underlying atomic structure, the Lorentz-4D analysis is complemented with local PDF line scans taken perpendicular to the shear band (Figure 12j). PDFs averaged over the left and right shear-band-affected zones (SBAZs) exhibit subtle, but systematic differences in the first and second peaks compared to each other and the undeformed matrix, indicating asymmetric changes in nearest-neighbor spacing and SRO across the band (Figure 12k). This asymmetry around the SB fits to the asymmetric SBAZs (Zr-depleted/Cu-rich versus Zr-enriched) previously observed by Mu et al.,[67] supporting the view that shear banding induces different nearest-neighbor and SRO changes on the tensile and compressive sides. Together, these results demonstrate that

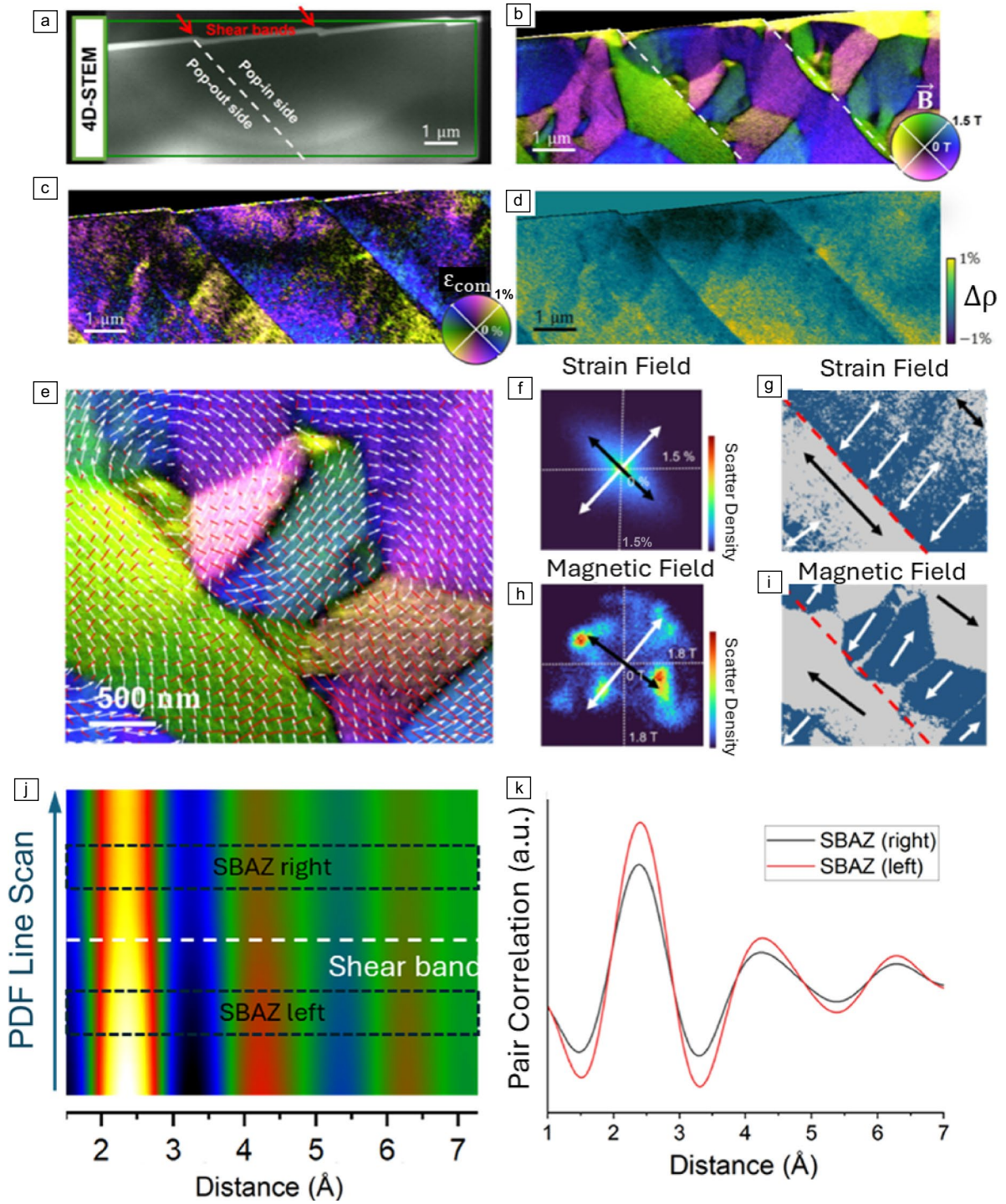

Figure 12. Large-angle Lorentz 4D scanning transmission electron microscopy (STEM) mapping of magnetic field, strain, density, and local structure around shear bands (SBs) in an $Fe_{85.2}Si_{0.5}B_{9.5}P_4Cu_{0.8}$ metallic glass. (a) Annular dark field (ADF)-STEM image of a lamella showing two SBs; the green frame marks the LA-Ltz-4D STEM scan area. (b) Map of the in-plane magnetic field $\vec{B}$ obtained from the shift of the first amorphous diffraction ring; the color encodes the field direction and brightness its magnitude. (c) Map of the compressive principal strain ϵ_{com}; the color code indicates the strain direction. (d) Relative density map $\Delta\rho$ derived from the integrated intensity of the first diffraction ring, highlighting local dilatation and compaction around the shear bands. (e) Combined view of magnetic and strain fields: white arrows show $\vec{B}$ and colored sticks ϵ_{com}, visualizing strong magnetoelastic coupling in the highly strained regions. (f, g) Representative 2D histogram of the tensile strain field and corresponding binarized map, illustrating two preferred strain orientations set by the SB geometry. (h, i) Analogous 2D histogram and binarized map for the magnetic field, revealing domains that follow the strain-induced anisotropy and domains dominated by magnetostatic interactions. (j) PDF line scan perpendicular to one SB, marking the left and right shear-band-affected zones (SBAZs) and the band core. (k) PDFs averaged over the left and right SBAZs, showing subtle, but systematic differences in nearest-neighbor distances and peak amplitudes that reflect asymmetric atomic packing across the SB. Panels adapted from Kang et al.[25]

multimodal 4D STEM analysis can simultaneously deliver maps of strain, density, magnetic field, and local pair correlations, enabling a direct correlation between atomic-scale packing motifs and functional responses such as magnetoelastic anisotropy in metallic glasses.

From PDF to 3D motifs: Atomic electron tomography of SRO and MRO

Atomic electron tomography (AET) is a real-space complement to total-scattering and PDF analysis.[71–74] Instead of inferring structure from an ensemble-averaged PDF, AET reconstructs 3D atomic coordinates in a nanoscale volume from an atomic-resolution STEM tilt series and then applies to the experimental coordinates the same correlation and topology tools that are widely used in atomistic simulations. This enables direct calculation of the PDF, partial pair correlations and higher-order descriptors such as Voronoi topology, bond-orientational order, and motif connectivity. Because AET is local, it can also map spatial heterogeneity in SRO and MRO that is averaged out in bulk PDF measurements.

In a landmark study,[30] Yang et al. determined the 3D atomic structure of an eight-element metallic-glass nanoparticle (Co, Ni, Ru, Rh, Pd, Ag, Ir, and Pt) using an ADF-STEM tilt series reconstructed by the RESIRE algorithm, followed by atom tracing and refinement (**Figure 13**). The final experimentally determined model contained 18,356 atoms and was chemically resolved at the level of three effective species by clustering ADF intensities (type 1: Co/Ni, type 2: Ru/Rh/Pd/Ag, type 3: Ir/Pt). Forward multislice validation indicated a 3D positional precision of about 21 pm and an overall atom identification accuracy of about 97 percent. From the disordered fraction of the nanoparticle, the authors computed the total PDFs and type-resolved partial PDFs,

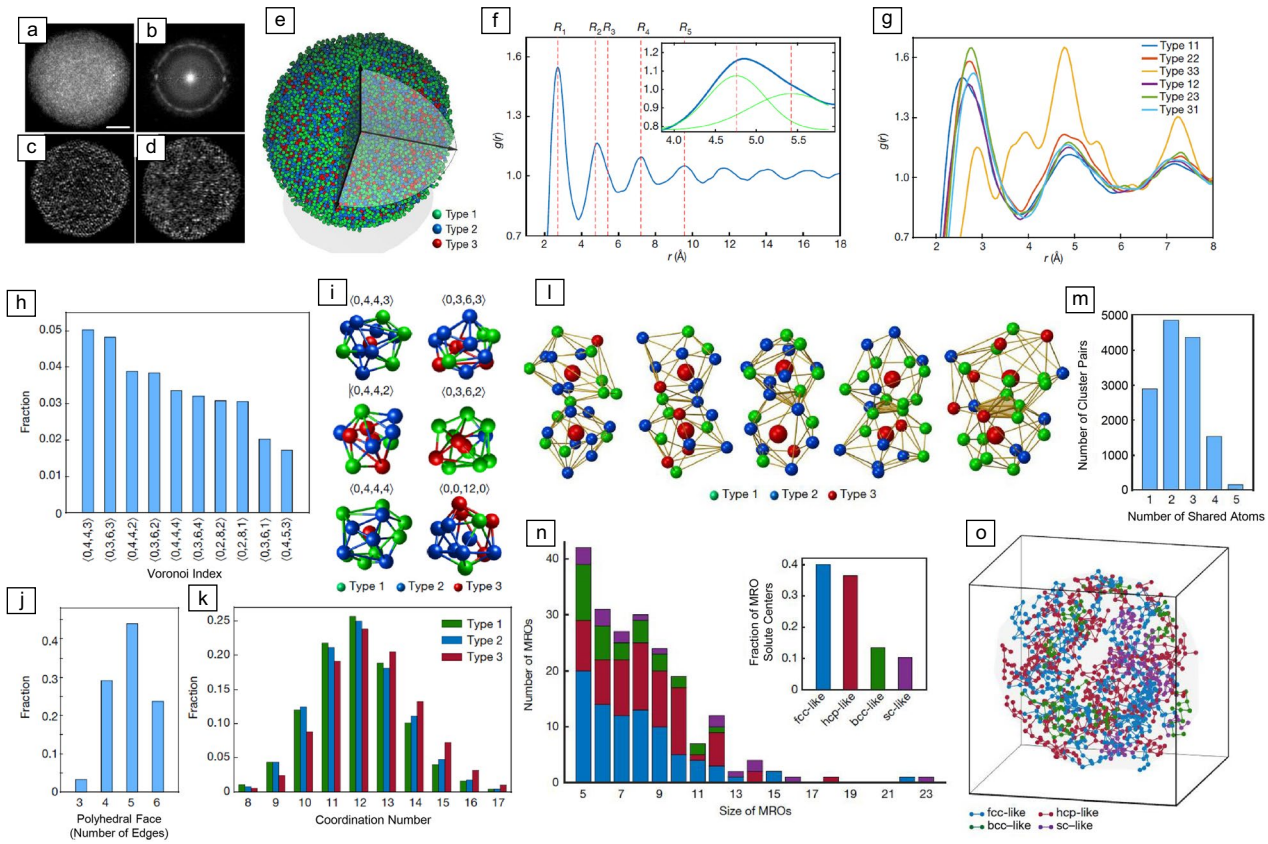

Figure 13. Atomic electron tomography (AET)-based pair distribution function (PDF) and topology analysis of short-range order (SRO) and medium-range order (MRO) in a multicomponent metallic-glass nanoparticle. (a) Annular dark-field (ADF)-scanning transmission electron microscopy STEM projection. (b) Power spectrum showing a diffuse amorphous ring. (c, d) Orthogonal slices through the 3D reconstruction. (e) 3D atomic model from AET, with atoms grouped into three Z-contrast classes (types 1–3). (f) Total PDF calculated from the coordinates, with coordination shells R_1–R_5 and split second peak (inset). (g) Partial PDFs for all type–type pairs. (h) Voronoi-index distribution for atoms in the amorphous matrix. (i) Representative chemically resolved SRO clusters. (j) Distribution of edges per Voronoi face, highlighting fivefold faces. (k) Coordination-number distributions for each type. (l) Representative MRO segments obtained by linking neighboring SRO clusters that share atoms. (m) Shared-atom connectivity between clusters. (n) MRO-domain size distribution and fraction of face-centered cubic (fcc)-like, hexagonal close-packed (hcp)-like, body-centered cubic (bcc)-like, and simple-cubic (sc)-like centers from bond-orientational order (inset). (o) Three-dimensional rendering of the interconnected MRO network colored by dominant crystal-like character. Adapted with permission from Reference 30. © 2021 Springer Nature.

showing metallic-glass features including a weak second-peak splitting (Figure 13f). The partial PDFs and Warren-Cowley analysis provided direct evidence of chemical SRO, with enhanced type-1–type-1 and type-2–type-3 bonding and suppressed type-1–type-2 and type-3–type-3 bonding (Figure 13g), trends that are difficult to isolate from bulk PDFs without strong model assumptions.

The power of AET is that it converts SRO from a set of averaged correlation peaks into explicit 3D motifs. Voronoi tessellation of the experimental coordinates shows that five-edged faces dominate the local topology, yet only a small fraction of Voronoi polyhedra are distorted icosahedra (Figure 13h–j). In this nanoparticle, five-edged faces account for about 44% of all faces, while distorted icosahedra account for about 7% of the polyhedra, and the mean coordination numbers are close to 12 (approximately 12.0, 12.0, and 12.4 for types 1–3) (Figure 13k). These quantitative results sharpen an important point for PDF-based discussions of glass structure: abundant fivefold signatures do not imply that icosahedral SRO is the dominant local motif.

Because the full 3D configuration is known, AET can also identify MRO as explicit networks of linked motifs (Figure 13l–m). Yang et al. experimentally identified the type-3 atoms as solute centers and used a breadth-first search criterion against ideal lattice-site templates to identify four coexisting crystal-like MRO superclusters (fcc-like, hcp-like, bcc-like, and simple-cubic-like (Figure 13n–o).[30] These MRO superclusters exhibit translational order but lack global orientational coherence, and they interconnect into an extended, nonperiodic backbone within the amorphous nanoparticle. Quantitatively, the nanoparticle contained 85 fcc-like, 71 hcp-like, 31 bcc-like, and 17 simple-cubic-like MRO superclusters (Figure 13n), with connectivity distributions that can be expressed in terms of how many atoms are shared between neighboring solute-center clusters.

A complementary AET study by Yuan et al. focused on monatomic amorphous metals,[29] including a sputtered Ta film and two Pd nanoparticles (**Figure 14**). After reconstructing the 3D atomic coordinates, crystalline nuclei were removed using a bond-orientational order metric, leaving purely amorphous regions for structural analysis. PDFs computed directly from the experimental coordinates agree well with molecular dynamics liquid Ta when distances are normalized by the first-neighbor peak position, consistent with the central conclusion of liquid-like packing in these monatomic amorphous solids (Figure 14c). Unlike multicomponent metallic glasses, these monatomic amorphous metals do not exhibit a pronounced second-peak splitting in the PDF (Figure 14f), highlighting that "amorphous" and "metallic glass" are not interchangeable categories.

With chemical complexity removed, Yuan et al. quantified the geometric building blocks of SRO and their extension into MRO.[29] Voronoi statistics again showed abundant five-edged faces (about 46%), but only about 10% distorted icosahedra (Figure 14d). The dominant motifs are polytetrahedral, especially pentagonal bipyramids. Using a tetrahedral distortion parameter δ to quantify how close local tetrahedra are to ideal, they showed that for modest distortion ($\delta \leq 0.255$) pentagonal bipyramids outnumber distorted icosahedra by orders of magnitude (17 versus 26,262 across the three experimental samples). Most pentagonal bipyramids connect into pentagonal-bipyramid networks (PBNs) by sharing vertices or edges, producing a direct real-space representation of MRO. In the Ta film, the largest PBN consisted of 135 pentagonal bipyramids formed by 165 atoms and extended to 2.83 nm. Because AET yields the full 3D tessellation, local mass density can be estimated from Voronoi volumes, and regions rich in polytetrahedral motifs are systematically denser than motif-poor regions by about 3% (Figure 14h–j). This establishes, experimentally and in three dimensions, a direct link between motif statistics, MRO network formation, and density heterogeneity.

Note that the atomic-position precision in AET for amorphous materials is approximately 21 pm,[29,30] which acts directly in real space and broadens the reconstructed pair-distance distribution. This broadening can reduce the apparent PDF peak heights and increase the peak widths. However, the intrinsic full width half maximum of the PDF in amorphous materials is typically much larger than the positional uncertainty. Therefore, the PDF linewidth broadening arising from the reconstruction uncertainty is low. As the AET volume is small, this represents very local PDF information.

Finally, advances in sub-angstrom electron ptychography point to a route for extending AET to thicker specimens and to amorphous materials with light element.[75] Ptychography reconstructs a phase image from coherent diffraction data and can be substantially more dose efficient than incoherent ADF imaging because it uses both unscattered and scattered electrons.[71,76] When combined with tomographic reconstruction, ptychographic AET (pAET) has the potential to improve 3D atomic localization and species sensitivity for light-element systems.[77,78] In a recent multislice benchmark simulation on a 6-nm amorphous SiO_2 nanoparticle, multislice pAET at 1.6×10^3 $e^-/Å^2$ per projection correctly identified 98.2% of Si and 96.7% of O, with 3D positional precisions of 10 pm–14 pm, respectively, while retaining medium-range structural information through ring statistics.[75] Together, ADF-based AET and pAET provide a pathway to experimentally determined 3D atomic coordinates that can be analyzed with PDF-style and topology-based tools to build an explicit real-space picture of SRO, MRO, and heterogeneity in amorphous materials.[71]

Outlook

PDF analysis has evolved into a common descriptor that connects bulk scattering, electron microscopy, and 3D imaging of amorphous materials. High-energy x-ray and neutron total scattering still provide the most robust PDFs, measuring average bond lengths, coordination numbers, and medium-range correlations in metallic glasses and related disordered alloys. These bulk measurements establish the structural parameter space within which local probes must operate and supply reference PDFs that are essential for validating models and for interpreting spatial variations.

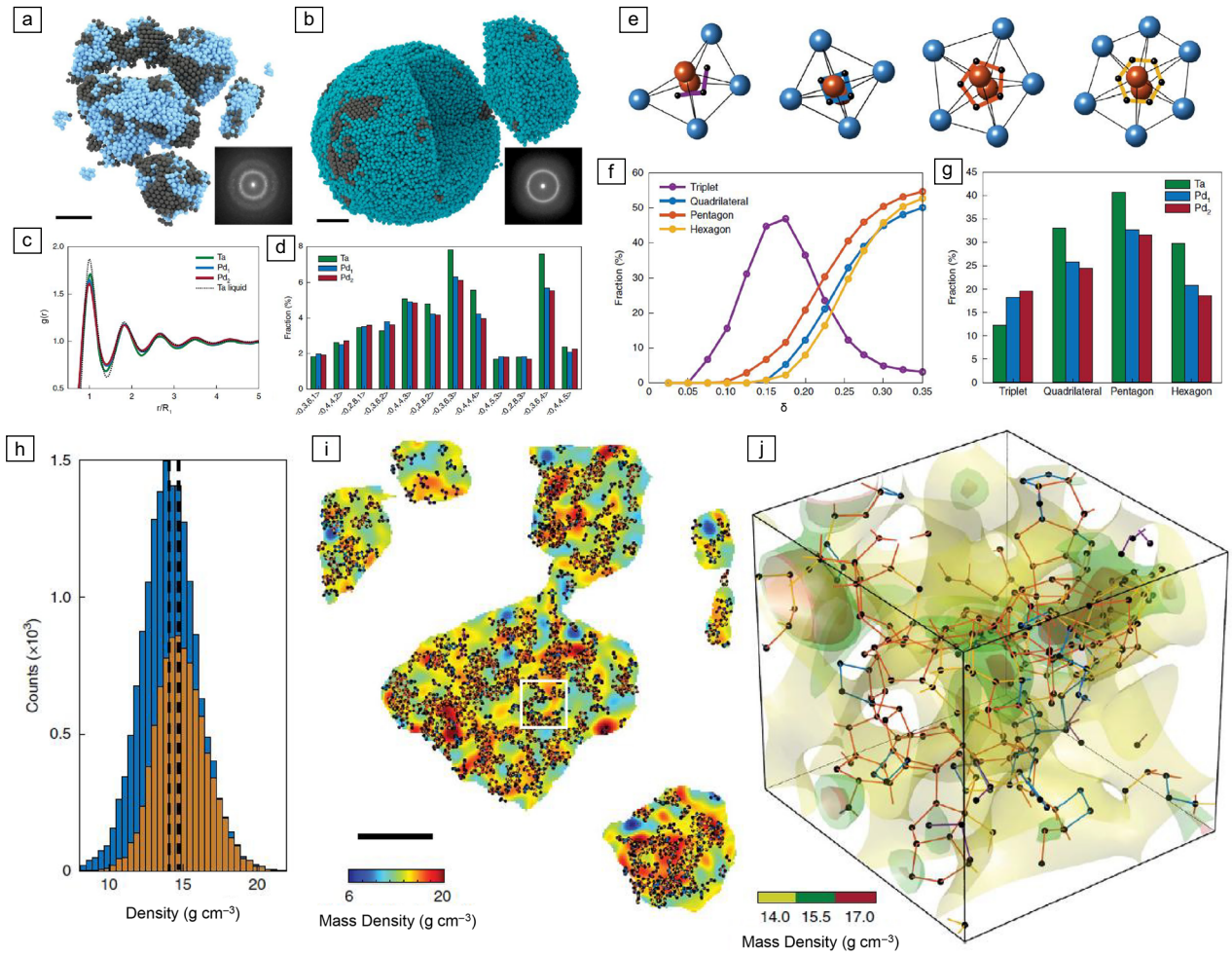

Figure 14. Atomic electron tomography (AET) of monatomic amorphous Ta and Pd: polytetrahedral packing and density heterogeneity. (a, b) Experimental 3D atomic models of an amorphous Ta thin film and a Pd nanoparticle (Pd_1), with surface crystalline nuclei in gray. Insets show averaged 2D power spectra with diffuse amorphous rings. (c) Pair distribution functions g(r) computed directly from the experimental coordinates for Ta, Pd_1, Pd_2, and a molecular dynamics-simulated Ta liquid, plotted versus r/R_1. (d) Fractions of the 12 most populated Voronoi polyhedra in the amorphous regions, labeled by Voronoi indices. (e) Dominant polytetrahedral motifs: triplet, quadrilateral, pentagonal, and hexagonal bipyramids, represented by three-, four-, five-, and sixfold skeletons connecting tetrahedral centroids. (f) Motif fraction in the Ta film as a function of the tetrahedral distortion parameter δ. (g) Motif fractions in Ta, Pd_1, and Pd_2 for $\delta \leq 0.255$. (h) Local mass-density distributions in Ta regions with (orange) and without (blue) polytetrahedral packing, showing an average density increase of about 3% in motif-rich regions. (i) Slice through the Ta film showing local mass density (color) overlaid with polytetrahedral packing (black). (j) Three-dimensional rendering of the boxed region in (i), overlaid with triplet (purple), quadrilateral (blue), pentagonal (orange), and hexagonal (yellow) skeletons. Panels adapted from Reference 29.

Electron microscopy builds on this foundation by combining PDF analysis with real space variations. Electron PDF in the TEM applies the same total-scattering formalism to thin foils and nanovolumes, after careful correction for multiple scattering and instrumental artefacts. Four-dimensional STEM records a diffraction pattern at every probe position, effectively turning each pixel into a local PDF measurement. The resulting PDF cube reveals how SRO and MRO vary across interfaces, in nanoglasses and in deformation microstructures. Multivariate and machine learning methods such as PCA, ICA, and NMF increase the information that can be retrieved for these complex structures. They allow to separate partially overlapping amorphous components, thus identifying a small set of basis PDFs (e.g., liquid-like and solid-like configurations), and provide quantitative maps of phase fractions and distributions, their correlation lengths, and motif populations. In this way, electron-based PDFs bridge the gap between ensemble-averaged bulk measurements and the nanoscale heterogeneity that underpins shear-banding, structural relaxation, and interfacial phenomena.

Three-dimensional imaging closes the loop by providing explicit atomic configurations from which PDFs and higher-order descriptors can be computed directly. Atomic electron tomography of multicomponent metallic-glass nanoparticles and monatomic amorphous metals has shown that it is now possible to reconstruct tens of thousands of atoms, calculate

total and partial PDFs from the experimental coordinates, and then analyze local polyhedra, cluster connectivity and density fields without assuming a particular structural model. These studies provide concrete local real-space realizations of ideas that previously came only from simulations or model fits to bulk PDFs: efficient cluster packing, crystal-like medium-range order, polytetrahedral backbones, and nanoscale density fluctuations.

A comparison of bulk PDF, ePDF, 4D STEM-PDF, and AET requires caution because the characteristic length scales obtained from these methods are related but not identical. In bulk x-ray or neutron PDF, the medium-range-order coherence length is typically extracted from the decay of PDF oscillations or from the width of the first sharp diffraction peak. It therefore represents a volume-averaged structural correlation length. In 4D STEM-PDF, the corresponding length scale more often describes the spatial correlation of PDF-derived components, motifs, or coefficient maps within a projected nanovolume. In AET, medium-range order can be evaluated directly from reconstructed atomic coordinates as the size, connectivity and topology of motif networks, polyhedral clusters, or crystal-like domains. Thus, these methods all quantify medium-range structural organization, but they probe different observables and different averaging volumes.

Finally, multimodal 4D STEM diffraction analysis enables simultaneous and correlated measurements of function properties, such as electric or magnetic fields, together with structural properties, such as strain and packing density, alongside the local PDFs. This demonstrates that structure–property correlations can be directly established within a single experiment and further even be combined with *in situ* measurements (5D-STEM).

Taken together, the methods reviewed here outline a coherent path toward a multiscale structural description of metallic glasses and other disordered materials. Bulk total scattering defines global averages and thermodynamic trends; electron-based PDFs reveal spatial variations in local order and functional properties; and 3D electron tomography provides direct atomic models. When combined with advanced data analysis and theory, this toolbox allows to follow how local packing motifs, medium-range networks and structural heterogeneity evolve during processing, deformation and relaxation with electron microscopy providing a quantitative structural description of amorphous structures.

Author contributions

C.K. and S.K. conceptualization, C.K., J.M., S.K., and T.E. funding acquisition, all authors visualization, S.K. writing – original draft, all authors writing – review and editing.

Funding

Open Access funding enabled and organized by Projekt DEAL. S.K. and C.K. acknowledge the support from the collaborative research centre FLAIR (Fermi level engineering applied to oxide electroceramics), which is funded by the German Research Foundation (DFG), Project-ID 463184206 – SFB 1548. S.K. acknowledges the support from the Technology Innovation Program (RS-2024–00418991) funded by the Ministry of Trade, Industry & Energy (MOTIE, Korea). S.K. and C.K appreciate the support received from the Joint Lab Model Driven Materials Characterization (MDMC) and acknowledge backing from the Helmholtz Imaging Project (HIP) BRLEMM. J.M. acknowledges support from the US Department of Energy, Office of Science, Basic Energy Sciences, Division of Materials Sciences and Engineering under Award DE-SC0010378, and STROBE: a National Science Foundation Science and Technology Center under Award DMR 1548924. T.E. was supported by the US Department of Energy, Office of Science, Basic Energy Sciences, Materials Sciences and Engineering Division.

Conflict of interest

The authors declare no conflict of interest or competing interests.

Open Access

References

1. Y. Cheng, E. Ma, *Prog. Mater. Sci.* **56**, 379 (2011)
2. J. Bernal, *Nature* **185**, 68 (1960)
3. P.J. Steinhardt, D.R. Nelson, M. Ronchetti, *Phys. Rev. Lett.* **47**, 1297 (1981)
4. T. Tomida, T. Egami, *Phys. Rev. B* **52**, 3290 (1995)
5. B.E. Warren, *X-ray Diffraction* (Courier, North Chelmsford, 1990)
6. G.S. Cargill III, "Structure of Metallic Alloy Glasses," in *Solid State Physics,* vol. 30 (Academic Press, 1975), pp. 227–320
7. D.O. Akamo, A.O. Ijaola, T.T. George, K. Page, D.J. Keffer, Y. Li, M. Goswami, T.J. LaClair, K. Gluesenkamp, O. Rios, *Eur. J. Mater.* **3**, 2150897 (2023)
8. S.J. Billinge, *Z. Kristallogr. Cryst. Mater.* **219**, 117 (2004)
9. D.B. Miracle, *Nat. Mater.* **3**, 697 (2004)
10. T. Fukunaga, K. Itoh, T. Otomo, K. Mori, M. Sugiyama, H. Kato, M. Hasegawa, A. Hirata, Y. Hirotsu, A. Hannon, *Intermetallics* **14**, 893 (2006)
11. J. Hwang, A.M. Clausen, H. Cao, P.M. Voyles, *J. Mater. Res.* **24**, 3121 (2009)
12. C. Liu, Z. Zhang, J. Ding, E. Ma, *Scr. Mater.* **225**, 115159 (2023)
13. D. Keen, R. McGreevy, *Nature* **344**, 423 (1990)
14. S. Luo, J.C. Khong, D. Daisenberger, S. Huang, P.F. McMillan, J. Mi, *Phys. Rev. B* **105**, 064203 (2022)
15. S. Luo, J.C. Khong, S. Huang, G. Yang, J. Mi, *Acta Mater.* **272**, 119917 (2024)
16. S. Huang, S. Luo, L. Qin, D. Shu, B. Sun, A.J. Lunt, A.M. Korsunsky, J. Mi, *Scr. Mater.* **211**, 114484 (2022)
17. S. Pan, J. Qin, W. Wang, T. Gu, *Phys. Rev. B* **84**, 092201 (2011)
18. M. Ghaemi, R. Tavakoli, A. Foroughi, *J. Non-Cryst. Solids* **499**, 227 (2018)
19. M. Celtek, S. Sengul, U. Domekeli, *Intermetallics* **84**, 62 (2017)

20. M. Li, C. Wang, S. Hao, M. Kramer, K. Ho, *Phys. Rev. B Condens. Matter Mater. Phys.* **80**, 184201 (2009)
21. T. Egami, W. Dmowski, C.W. Ryu, *Metals* (Basel) **13**, 442 (2023)
22. C. Ophus, *Microsc. Microanal.* **25**, 563 (2019)
23. J. Hwang, Z. Melgarejo, Y.E. Kalay, I. Kalay, M.J. Kramer, D. Stone, P. Voyles, *Phys. Rev. Lett.* **108**, 195505 (2012)
24. S. Kang, V. Wollersen, C. Minnert, K. Durst, H.-S. Kim, C. Kübel, X. Mu, *Acta Mater.* **263**, 119495 (2024)
25. S. Kang, M. Töllner, D. Wang, C. Minnert, K. Durst, A. Caron, R.E. Dunin-Borkowski, J. McCord, C. Kübel, X. Mu, *Nat. Commun.* **16**, 1305 (2025)
26. S. Kang, D. Wang, A. Caron, C. Minnert, K. Durst, C. Kübel, X. Mu, *Adv. Mater.* **35**, 2212086 (2023)
27. X. Mu, A. Mazilkin, C. Sprau, A. Colsmann, C. Kübel, *Microscopy* **68**, 301 (2019)
28. X. Mu, S. Neelamraju, W. Sigle, C.T. Koch, N. Toto, J.C. Schön, A. Bach, D. Fischer, M. Jansen, P.A. van Aken, *J. Appl. Crystallogr.* **46**, 1105 (2013)
29. Y. Yuan, D.S. Kim, J. Zhou, D.J. Chang, F. Zhu, Y. Nagaoka, Y. Yang, M. Pham, S.J. Osher, O. Chen, P. Ercius, A.K. Schmid, J. Miao *Nat. Mater.* **21**, 95 (2022)
30. Y. Yang, J. Zhou, F. Zhu, Y. Yuan, D.J. Chang, D.S. Kim, M. Pham, A. Rana, X. Tian, Y. Yao, S. Osher, A.K. Schmid, L. Hu, P. Ercius, J. Miao, *Nature* **592**, 60 (2021)
31. T. Egami, S.J.L. Billinge, *Underneath the Bragg Peaks: Structural Analysis of Complex Materials,* 2nd edn., Pergamon Materials Series, vol. 16 (Newnes, 2012)
32. P.J.W. Debye, *Über den Einfluss der Wärmebewegung auf die Interferenzerscheinungen bei Röntgenstrahlen* (Druck von Friedr. Vieweg & Sohn, 1913)
33. T. Egami, "Atomistic Theory of Metallic Liquids and Glasses," in *Bulk Metallic Glasses,* ed. by M. Miller, P. Liaw (Springer, New York, 2008), pp. 27–55
34. P. Fuoss, P. Eisenberger, W. Warburton, A. Bienenstock, *Phys. Rev. Lett.* **46**, 1537 (1981)
35. J. Enderby, *Annu. Rev. Phys. Chem.* **34**, 155 (1983)
36. C.W. Ryu, W. Dmowski, K. Kelton, G. Lee, E. Park, J. Morris, T. Egami, *Sci. Rep.* **9**, 18579 (2019)
37. T. Egami, C.W. Ryu, *Front. Mater.* **9**, 874191 (2022)
38. C.W. Ryu, T. Egami, *J. Chem. Phys.* **162**, 234501 (2025)
39. P.S. Salmon, A. Zeidler, *J. Stat. Mech.* **2019**, 114006 (2019)
40. T. Egami, C.W. Ryu, *J. Phys. Condens. Matter* **35**, 174002 (2023)
41. T. Egami, C.W. Ryu, *AIP Adv.* **13**, 085308 (2023)
42. S. Alexander, J. McTague, *Phys. Rev. Lett.* **41**, 702 (1978)
43. D. Shechtman, I. Blech, D. Gratias, J.W. Cahn, *Phys. Rev. Lett.* **53**, 1951 (1984)
44. T. Egami, C.W. Ryu, *J. Appl. Phys.* **137**, 070901 (2025)
45. T. Egami, C.W. Ryu, *Phys. Rev. E* **104**, 064110 (2021)
46. T. Egami, C.W. Ryu, *Front. Chem.* **8**, 579169 (2020)
47. T. Egami, Y. Tong, W. Dmowski, *Metals* (Basel) **6**, 22 (2016)
48. C.W. Ryu, T. Egami, *Phys. Rev. E* **102**, 042615 (2020)
49. Y.P. Mitrofanov, M. Peterlechner, I. Binkowski, M.Y. Zadorozhnyy, I. Golovin, S. Divinski, G. Wilde, *Acta Mater.* **90**, 318 (2015)
50. L. Zella, J. Moon, T. Egami, *Nat. Commun.* **15**, 1358 (2024)
51. P.W. Anderson, B.I. Halperin, C.M. Varma, *Philos. Mag.* **25**, 1 (1972)
52. T. Egami, *Mater. Sci. Eng. A* **226**, 261 (1997)
53. T. Egami, S. Poon, Z. Zhang, V. Keppens, *Phys. Rev. B Condens. Matter Mater. Phys.* **76**, 024203 (2007)
54. G. Li, K.B. Borisenko, Y. Chen, D. Nguyen-Manh, E. Ma, D.J. Cockayne, *Acta Mater.* **57**, 804 (2009)
55. G. Anstis, Z. Liu, M. Lake, *Ultramicroscopy* **26**, 65 (1988)
56. J. Ankele, J. Mayer, P. Lamparter, S. Steeb, *Z. Naturforsch. A* **60**, 459 (2005)
57. S. Kang, H. Cho, M. Töllner, V. Wollersen, D. Wang, H. Baik, M.J. Perera, O. Adjaoud, K. Albe, C. Kübel, *Ultramicroscopy* **281**, 114295 (2025)
58. X. Mu, L. Chen, R. Mikut, H. Hahn, C. Kübel, *Acta Mater.* **212**, 116932 (2021)
59. X. Mu, D. Wang, T. Feng, C. Kübel, *Ultramicroscopy* **168**, 1 (2016)
60. Y. Rakita, J.L. Hart, P.P. Das, S. Shahrezaei, D.L. Foley, S.N. Mathaudhu, S. Nicolopoulos, M.L. Taheri, S.J. Billinge, *Acta Mater.* **242**, 118426 (2023)
61. S. Hilke, H. Rösner, D. Geissler, A. Gebert, M. Peterlechner, G. Wilde, *Acta Mater.* **171**, 275 (2019)
62. O. Vaerst, H. Rösner, M. Peterlechner, G. Wilde, *J. Alloys Compd.* **1051**, 186051 (2026). https://doi.org/10.1016/j.jallcom.2026.186051
63. F.A. Davani, S. Hilke, H. Rösner, D. Geissler, A. Gebert, G. Wilde, *J. Appl. Phys.* **128**, 015103 (2020)
64. J. Hwang, A.M. Clausen, H. Cao, P.M. Voyles, *J. Mater. Res.* **24**, 3121 (2009)
65. J. Hwang, Z.H. Melgarejo, Y.E. Kalay, I. Kalay, M.J. Kramer, D.S. Stone, P.M. Voyles, *Phys. Rev. Lett.* **108**, 195505 (2012)
66. P. Zhang, J.J. Maldonis, M.F. Besser, M.J. Kramer, P.M. Voyles, *Acta Mater.* **109**, 103 (2016)
67. X. Mu, M.R. Chellali, E. Boltynjuk, D. Gunderov, R.Z. Valiev, H. Hahn, C. Kübel, Y. Ivanisenko, L. Velasco, *Adv. Mater.* **33**, 2007267 (2021)
68. F.A. Davani, S. Hilke, H. Rösner, D. Geissler, A. Gebert, G. Wilde, *J. Alloys Compd.* **837**, 155494 (2020)
69. C. Gammer, C. Ophus, T.C. Pekin, J. Eckert, A.M. Minor, *Appl. Phys. Lett.* **112**, 171905 (2018)
70. S. Kang, D. Wang, C. Kübel, X. Mu, *Ultramicroscopy* **255**, 113844 (2024)
71. J. Miao, *Nature* **637**, 281 (2025)
72. J. Miao, P. Ercius, S.J.L. Billinge, *Science* **353**(6306), aaf2157 (2016)
73. J. Zhou, Y. Yang, Y. Yang, D.S. Kim, A. Yuan, X. Tian, C. Ophus, F. Sun, A.K. Schmid, M. Nathanson, H. Heinz, Q. An, H. Zeng, P. Ercius, J. Miao, *Nature* **570**, 500 (2019)
74. S. Moniri, Y. Yang, J. Ding, Y. Yuan, J. Zhou, L. Yang, F. Zhu, Y. Liao, Y. Yao, L. Hu, P. Ercius, J. Miao, *Nature* **624**, 564 (2023)
75. Y. Liao, H. Sha, C.M. O'Leary, H. Zhong, Y. Yang, J. Miao, *Nature* **649**, 1123 (2026)
76. Z. Chen, Y. Jiang, Y.-T. Shao, M.E. Holtz, M. Odstrčil, M. Guizar-Sicairos, I. Hanke, S. Ganschow, D.G. Schlom, D.A. Muller, *Science* **372**(6544), 826 (2021)
77. D.J. Chang, D.S. Kim, A. Rana, X. Tian, J. Zhou, P. Ercius, J. Miao, *Phys. Rev. B* **102**, 174101 (2020)
78. P.M. Pelz, S.M. Griffin, S. Stonemeyer, D. Popple, H. DeVyldere, P. Ercius, A. Zettl, M.C. Scott, C. Ophus, *Nat. Commun.* **14**, 7906 (2023) □

Sangjun Kang is working at the Karlsruhe Institute of Technology (KIT), Germany, and the Technical University of Darmstadt (TUD), Germany, on multidimensional electron microscopy, including four-dimensional-scanning transmission electron microscopy, for materials characterization and reliability/failure analysis. He received his PhD degree from TUD in 2023, after completing research at KIT. His research spans electron pair distribution function (ePDF) analysis, amorphous characterization, oxide electroceramics, and advanced transmission electron microscopy methodology. Kang can be reached by email at sangjun.kang@tu-darmstadt.de.

Hyeyoung Cho is a doctoral researcher at the Technical University of Darmstadt (TUD), Germany, and conducts research at the Karlsruhe Institute of Technology (KIT), Germany. Her work focuses on integrating four-dimensional-scanning transmission electron microscopy techniques, including electron pair distribution function analysis orientation and strain mapping, differential phase contrast, and enegy-dispersive x-ray spectroscopy/electron energy-loss spectroscopy, with *in situ* transmission electron microscopy to investigate structure–property correlations in functional materials. Cho can be reached by email at hyeyoung.cho@tu-darmstadt.de.

Takeshi Egami has been the UT-ORNL Distinguished Scientist/Professor at The University of Tennessee, Knoxville, and Oak Ridge National Laboratory (UT-ORNL) since 2003. He taught at the University of Pennsylvania from 1973 to 2003. His research fields include liquid and glass, effects of dynamic and static disorder in crystals, and neutron and x-ray scattering. He published a book (*Underneath the Bragg Peaks: Structural Analysis of Complex Materials,* Elsevier, 2003, 2012), and more than 600 technical papers. He is the editor of *Advances in Physics*. Egami can be reached by email at egami@utk.edu.

Yuxuan Liao is a postdoctoral fellow in the Department of Physics and Astronomy at the University of California, Los Angeles. He received his PhD degree from The University of Tokyo, Japan. His research focuses on exploring novel phonon and electron physics in complex nanostructured crystalline and amorphous materials, as well as developing and applying advanced characterization techniques, including inelastic x-ray and neutron scattering, and atomic electron tomography. Liao can be reached by email at whuarxuan@gmail.com.

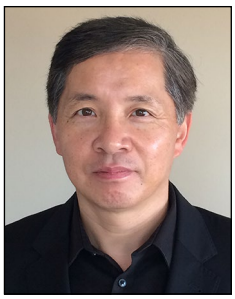

Jianwei Miao is professor of physics and astronomy at the University of California, Los Angeles, and a member of the California NanoSystems Institute. He received a MS degree from the Chinese Academy of Sciences in 1994 and a PhD degree in physics from Stony Brook University, The State University of New York in 1999. He pioneered computational microscopy by unifying crystallography and microscopy through coherent diffraction and algorithms. As a graduate student, he carried out the first experimental demonstration of coherent diffractive imaging, extending x-ray crystallography from crystals to noncrystalline specimens and laying the foundation for modern ptychography. He later pioneered atomic electron tomography, which enabled three-dimensional (3D) atomic imaging without assuming crystallinity, and in 2021, he and his collaborators reported the first determination of the 3D atomic structure of an amorphous solid. He is an American Physical Society (APS) Fellow and Materials Research Society (MRS) Fellow, and a recipient of the 2021 MRS Innovation in Materials Characterization Award and the 2026 APS Joseph F. Keithley Award for Advances in Measurement Science. Miao can be reached by email at j.miao@ucla.edu.

Christian Kübel is professor of *in situ* electron microscopy at the Technical University of Darmstadt (TUD), Germany, and research unit chair for advanced electron microscopy in materials research at Karlsruhe Institute of Technology, Germany, since 2019. He received his PhD degree in chemistry in 1998 working at the Max Planck Institute for Polymer Research, Germany. After completing postdoctoral research at the University of Michigan, he worked as a senior application specialist at Philips/FEI. In 2009, he began at the Karlsruhe Institute of Technology, Germany, where he is currently deputy director of the Karlsruhe Nano Micro Facility (KNMFi). His research is focused on electron microscopy developments for applications in materials science. Kubel can be reached by email at christian.kuebel@kit.edu.